A decade of short-period earthquake rupture histories from multi-array back-projection

Felipe Vera[1,2], Frederik Tilmann[1,2]& Joachim Saul[1]

[1]German Research Centre for Geosciences GFZ, Albert-Einstein-Straße 42-46, 14473, Potsdam, Germany.

[2]Institute for Geological Sciences, Freie Universität Berlin, Malteserstraße 74-100, 12249, Berlin, Germany.

Key Points:

- We provide a complete catalog of high-frequency rupture histories for M≥7.5 events 2010-2021.
- We develop a semi-automatic method for estimating rupture length, speed, directivity, and aspect ratio.
- Asperity encircling ruptures and emissions up-dip of main asperity common in large megathrust earthquakes.

Corresponding author: Felipe Vera, `fvera@gfz-potsdam.de`

Abstract

Teleseismic back-projection has emerged as a widely-used tool for understanding the rupture histories of large earthquakes. However, its application often suffers from artifacts related to the receiver array geometry, notably the 'swimming' artifact. We present a teleseismic back-projection method with multiple arrays and combined P and pP waveforms. The method is suitable for defining arrays ad-hoc in order to achieve a good azimuthal distribution for most earthquakes. We present a catalog of short-period rupture histories (0.5–2.0 Hz) including all 54 earthquakes from 2010 to 2021 with $M_W \geq 7.5$ and depth less than 200 km. The method provides semi-automatic estimates of rupture length, directivity, speed, and aspect ratio, which are related to the complexity of large ruptures. We determined short-period rupture length scaling relations that are in good agreement with previously published relations based on estimates of total slip. Rupture speeds were consistently in the sub-Rayleigh regime for thrust and normal earthquakes, whereas a tenth of strike-slip events propagated in the unstable supershear range. Many of the rupture histories exhibited complex behaviors such as rupture on conjugate faults, bilateral ruptures, and dynamic triggering by a P wave. For megathrust earthquakes, ruptures encircling asperities were frequently observed, with down-dip, up-dip, double encircling, and segmented patterns. Although there is a preference for short-period emissions to emanate from central

and down-dip parts of the megathrust, emissions up-dip of the main asperities are more frequent than suggested by earlier results.

Plain Language Summary

Back-projection is an earthquake imaging method based on seismic waveforms recorded remotely at a group of seismometers (seismic array). We present a new approach that combines waveforms of multiple seismic arrays to improve spatial resolution. We provide a catalog of large earthquake rupture histories from 2010 to 2021, producing a map view of the high-frequency radiation emitted along the fault plane. The method estimates semi-automatic earthquake rupture length, speed, directivity, and aspect ratio. Based on these estimates, we determined scaling relations between earthquake magnitude and rupture length that agree with classical relationships. We identified several strike-slip earthquakes propagating at supershear, i.e., faster than the shear wave speed, the usual limit for self-sustaining rupture propagation. We observed complex rupture behaviors, e.g., multiple faults activated, bilateral ruptures, and triggering of the main phase of a rupture by a primary (P) wave from the earliest part of the rupture. For subduction earthquakes, high-frequency emission points were often observed forming a ring around the fault interface patches (asperities) where the main slip occurs. There is a preference for high-frequency emissions to emanate

from central and deeper parts of the subduction plate interface, but shallower emissions are more frequent than expected from previous literature.

1 Introduction

Since the 26 December 2004 Sumatra-Andaman (M_W 9.1) earthquake, back-projection rupture imaging has become a complementary method to finite-fault source inversions for determining the kinematics of very large ruptures (e.g., Krüger & Ohrnberger, 2005; Ishii et al., 2005; Walker et al., 2005). Back-projection exploits the coherence of (usually) teleseismic P waveforms with limited prior assumptions on the fault geometry. Applications have targeted, for example, megathrust subduction earthquakes (e.g., Lay et al., 2010; Palo et al., 2014; Meng et al., 2011; Koper et al., 2011), aftershock detection (e.g., Kiser & Ishii, 2013; Feng et al., 2020; Tilmann et al., 2016), complex ruptures along multiple faults (e.g., Meng et al., 2012a; Lay et al., 2018; Ruppert et al., 2018), intermediate-depth earthquakes (e.g., Kiser et al., 2011; Ye et al., 2020), moderate size earthquakes (e.g., D'Amico et al., 2010; Taymaz et al., 2021), and near-field tsunami prediction (e.g., An & Meng, 2016; Xie & Meng, 2020), among others.

Back-projection is generally applied to large earthquakes. It uses short-period filtered waveforms, which can resolve details of the earthquake rupture better than long-period waveforms (e.g., Kiser & Ishii, 2017). The frequency band must be considered in the interpretation of the inferred rupture history. Short-period radiation is related to variations of slip and rupture velocity (e.g., Madariaga, 1983, 1977; Marty et al., 2019). This implies

that the back-projected rupture history can be related to fault heterogeneities. For example, subduction zone megathrust earthquakes were found to radiate short-period energy predominantly in deeper parts of the megathrust, down-dip of the maximum slip regions derived from finite-fault inversions, which are sensitive to the low-frequency behavior of the rupture (e.g., Lay et al., 2012; Yao et al., 2011, 2013). The apparently dominant down-dip short-period radiation is proposed to occur at the transition between brittle and ductile regions (e.g., Simons et al., 2011; Lay et al., 2012). Recently, Wang et al. (2020) correlated the 27 February 2010 Maule (M_W 8.8) earthquake short-period rupture with down-dip segmentation at the base of the overriding mantle wedge. In contrast to this view of the along-dip segmentation of seismic emission during large earthquakes, Meng et al. (2018) provided the first evidence for an encircling rupture, with high-frequency emissions both up-dip and down-dip of the main slip patch for the 16 September 2015 Illapel (M_W 8.3) earthquake. This observation is in contrast to earlier back-projection studies for this earthquake, which had shown the expected, predominantly down-dip rupture pattern (e.g., Melgar et al., 2016; Tilmann et al., 2016; Yin et al., 2016). It raises the question if this type of complex behavior is actually more common and just requires higher resolution rupture images.

Fracture mechanics predicts that instabilities such as earthquakes either propagate at sub-Rayleigh speed or exceed the shear wave speed (e.g., Burridge, 1973; Andrews, 1976; Das & Aki, 1977), where the latter is only expected for mode II cracks. In mode II cracks the

rupture propagates in the direction of displacement, which is also the direction of the initial shear stress resolved onto the fault. Such supershear earthquakes are associated with simple fault geometry and homogeneous stress-strength conditions (e.g., Bouchon et al., 2010), but also to damage zones under relatively low stress leading to unstable supershear ruptures, that is, between the shear wave speed and $\sqrt{2}$ times the shear wave speed (e.g., Burridge et al., 1979). Many strike-slip earthquakes with supershear speeds have been reported in the literature, see Robinson et al. (2010) for a review, e.g., the 1979 Imperial Valley (e.g., Archuleta, 1984; Spudich & Cranswick, 1984), 1999 Izmit (e.g., Bouchon et al., 2001), 2002 Denali (e.g., Dunham & Archuleta, 2004; Walker & Shearer, 2009), 2001 Kunlunshan (e.g., Bouchon & Vallée, 2003), 2013 Craig (e.g., Aderhold & Abercrombie, 2015; Yue et al., 2013) and the 2018 Palu earthquake (e.g., Bao et al., 2019; Socquet et al., 2019).

A disadvantage of the back-projection method is that the array configuration can cause notable artifacts in the recovered rupture (e.g., Meng et al., 2012b). Back-projection often leads to a persistent time-space trade-off of the earthquake rupture towards the seismic array, often called 'swimming' artifact. The swimming artifact arises from the low curvature of the time-distance travel time curve. Sources closer to the receivers but activated later will have the same arrival time as earlier sources farther away, resulting in a point source in space and time to appear as an extended source drifting towards the array. In animations showing the evolution of the back-projected energy with time, this slightly irregular drifting

looks like a swimming motion, giving the artifact its name. Because of the dependence on the array azimuth, it is easy to understand why the swimming artifact can be reduced by combining multiple array images.

Depth phases can cause additional artifacts in the form of 'ghost' emitters corresponding approximately to the bounce points of the surface-reflected phase, but they also can carry additional information. For large intermediate-depth earthquakes, the time-delay between P and depth phases (e.g., pP and sP) allowed to improve the resolution in depth by combining both P and depth phase backprojections (e.g., Kiser et al., 2011). For more shallow earthquakes (40–100 km), depth phases can contribute significantly to uncertainties (e.g., Zeng et al., 2019). To our knowledge, however, a systematic imaging method that integrates depth phases and multiple arrays for the shallow depth range has not been reported yet.

This study presents such a method and its application to derive a catalog of rupture histories of recent large earthquakes (2010 to October 2021) in the 0.5–2.0 Hz frequency range, which is complete for $M_W \geq 7.5$ and depths less than 200 km. Specifically, we extended the multi-array approach of Rössler et al. (2010) and included depth phases (for earthquakes deeper than 40 km) and weighted seismic array images. We provide an algorithm for automatically estimating rupture length, directivity, speed, and aspect ratio from

back-projection results. Short-period rupture lengths were used to calculate scaling relations and compare them to established relationships. The analysis focuses on complex ruptures and depth-varying short-period radiation for large subduction earthquakes and the detection of supershear ruptures for strike-slip events. We also show that short-period ruptures encircling asperities, as observed for the 2015 Illapel earthquake in Chile, are frequent in subduction megathrust earthquakes. The results suggest that short-period rupture complexities, e.g., encircling rupture around slip patches, are related to asperity stress conditions (and seismogenic barriers) rather than the overall along-dip megathrust segmentation.

2 Methods

2.1 Multi-Array Multi-Phase Back-Projection

The back-projection method is similar to beamforming in maximizing the coherency of time-shifted waveforms at an array. Unlike in beamforming, there is no assumption of a planar wavefield. Instead, the time shifts are calculated from the predicted travel times for a grid spaced around the hypocenter. In practice, the grid is usually two-dimensional, chosen to be either a horizontal plane at the hypocentral depth, or a plane aligned with one of the nodal planes of the focal mechanism, or an *a priori* known fault surface, e.g., the slab interface in subduction zones. The waveforms are back-projected onto this grid. The theoretical arrival of a target seismic wave (e.g., P wave) based on a reference velocity

model controls the beamforming delays. For each grid point, the resulting array beam is:

$$b_i(t) \quad = \quad \frac{1}{N_k} \sum_{k=1}^{N_k} u_k(t + t_{ik} + \Delta t_k) \ , \tag{1}$$

where $b_i(t)$ is the beam for the ith grid point, u_k the vertical component waveform recorded at station k, t_{ik} the travel time between the grid-point i and station k in a reference velocity model, and Δt_k the station-specific static correction term accounting for differences between the reference and true velocity model.

The station correction terms can, to a large extent, absorb the effect of 3D Earth heterogeneities on arrival times. They are usually determined by cross-correlating the first few seconds of the rupture recorded by each receiver. The resulting time-shifted arrivals are then compared to those predicted for the catalog hypocenter, and the differences correspond to the necessary correction terms. Thus, the back-projection image retrieves the rupture nucleation at the catalog hypocenter by definition. For very large earthquakes, aftershocks can alternatively be used to correct source-receiver paths away from the hypocenter (e.g., Ishii et al., 2007; Palo et al., 2014; Meng et al., 2016). The advantage over the hypocenter-based calibration is that the location errors of several events are averaged, such that a possible bias from mislocation of the mainshock hypocenter is reduced and furthermore spatially varying station terms due to 3D structure effects can be accommodated. The calibration with aftershocks is particularly important when the rupture pattern is compared

with aftershocks. In contrast, the mainshock calibration offers advantages in near-real-time applications with automatic routines since only the hypocenter is required. For simplicity, in this work, we adopt the hypocenter calibration, but it would be easy to adopt the method to aftershock calibration. Alternatively, travel calculations could be performed in a 3D Earth model (e.g., Liu et al., 2017).

In order to carry out the actual rupture tracking, the maxima of beamformed energy ($\mathbf{E_i}$) and semblance ($\mathbf{S_i}$), defined in equations (2) and (3) below, are used to locate the most intense emission at each time step. The energy represents the amount of radiation emitted, and semblance provides a measure of the coherence of waveforms which is not affected by the amplitudes of individual traces and is, therefore, more effective for tracking the location of earthquake rupture (e.g., Neidell & Taner, 1971; Rössler et al., 2010; Palo et al., 2014). For both measures, a time window of length W needs to be defined, which should contain at least two periods of the longest period analyzed.

$$\mathbf{E_i}(t) = \int_t^{t+W} \left|\mathbf{b_i}(\tau)\right|^2 d\tau \tag{2}$$

$$\mathbf{S_i}(t) = \frac{1}{N} \frac{\mathbf{E_i}(t)}{\int_t^{t+W} [\sum_{k=1}^{N_k} \mathbf{u_k^2}(\tau + t_{ik} + \Delta t_k)] d\tau} \tag{3}$$

Both measures provide an image of the earthquake rupture. Given a grid of sources, the tracking of the local semblance maxima provides a way to map the rupture propagation. The energy peak in each time window provides a relative measure of the source time function

of short-period seismic energy, which is related to but not necessarily proportional to the moment rate, e.g., as derived from finite fault solutions. We also note that the absolute values of the energy function depend on the array configurations, and a comparison of the absolute energy amplitudes is not physically meaningful unless the same arrays are utilized, but that the time history for any given earthquake is related to the physical rupture process. The time-integrated energy maps thus provide a summary view of the high-frequency energy radiation.

For the processing of data from multiple arrays, we initially follow the approach from Rössler et al. (2010) where semblance and energy maps from N_a arrays are multiplied to provide the rupture and energy radiated, respectively:

$$\hat{\mathbf{E}}_\mathbf{i}(t) = \prod_{a=1}^{N_a} \mathbf{E}_\mathbf{i}(t) \tag{4}$$

$$\hat{\mathbf{S}}_\mathbf{i}(t) = \prod_{a=1}^{N_a} \mathbf{S}_\mathbf{i}(t) \tag{5}$$

Here, we introduce two modifications: (i) we use exponents (equivalent to weights in log-space) to balance the contributions of individual arrays based on their azimuthal distribution in order to avoid artifacts due to clustering of arrays in certain azimuthal ranges, and (ii) for earthquakes deeper than 40 km, we combine P and pP backprojections to reduce artifacts related to the depth phase (see Fig. 1a). The modified expressions are:

$$\hat{\mathbf{E}}_\mathbf{i}(t) = \prod_{a=1}^{N_a} \left[\prod_{p=1}^{N_p} f(t - t_0) \cdot \mathbf{E}_\mathbf{i}(t) \right]^{\gamma_a} \tag{6}$$

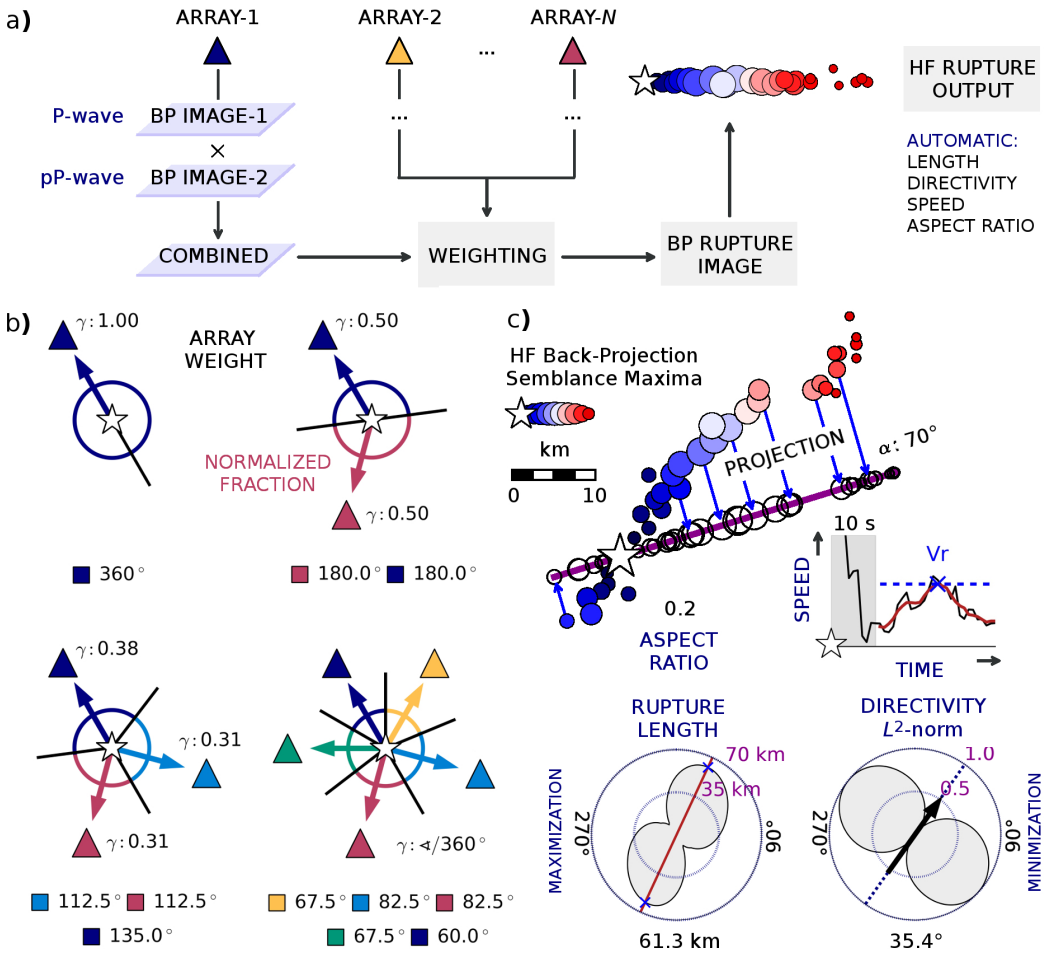

Figure 1. Multi-array multi-phase back-projection. a) Workflow for rupture imaging using P and pP waveform arrivals and multiple seismic arrays. pP arrivals are only included for earthquakes with depth $\geq$ 40 km. The last step contains the extraction of a few rupture parameters based on the timing and locations of rupture maxima. b) Array weighting. The sum of azimuthal half-angles between the target and its two neighboring arrays is proportional to the weights γ. c) Automatic estimation of the rupture aspect ratio, speed, length, and directivity; see text for details.

$$\hat{\mathbf{S}}_{\mathbf{i}}(t) \quad = \quad \prod_{a=1}^{N_a} \left[\prod_{p=1}^{N_p} f(t - t_0) \cdot \mathbf{S}_{\mathbf{i}}(t) \right]^{\gamma_a} \tag{7}$$

We assign $p = 1$ to P and $p = 2$ to pP waveforms, and N_P is the number of phases used. Here $N_p = 1$ is used for shallow earthquakes and 2 for deep earthquakes, but the method is open to experimenting with alternate seismic wave arrivals. The weighting exponent γ is set proportionally to the sum of the two half-angles between the azimuths of target and neighboring arrays (see Fig. 1b), where the median of the array receiver coordinates is assumed to be the reference location for the weighting estimation, and the normalization is chosen such that $\sum_i^{N_a} \gamma_i = 1$. Therefore, for a single array $\gamma = 1$, and for two, we always have $\gamma = 0.5$, but for irregularly distributed arrays, the weighting depends on the distribution. The term $f(t-t_0)$, with t_0 the origin time of the earthquake, is a taper function adapted from Kiser et al. (2011) to mute the waveform before the first arrival when multiple seismic phases are included:

$$f(\tau) = \begin{cases} 0 & \text{for } \tau \leq -T/2 \\ \frac{1}{2}\left[\cos\left(\frac{2\tau\pi}{T}\right) + 1\right] & \text{for } -T/2 < \tau < 0 \\ 1 & \text{for } \tau \geq 0 \end{cases} \tag{8}$$

If $\tau = 0$, the rupture has initiated, and the results are fully incorporated to image the source; otherwise, they are suppressed. T is the period of the cosine taper function controlling the transition between admitted and suppressed intervals.

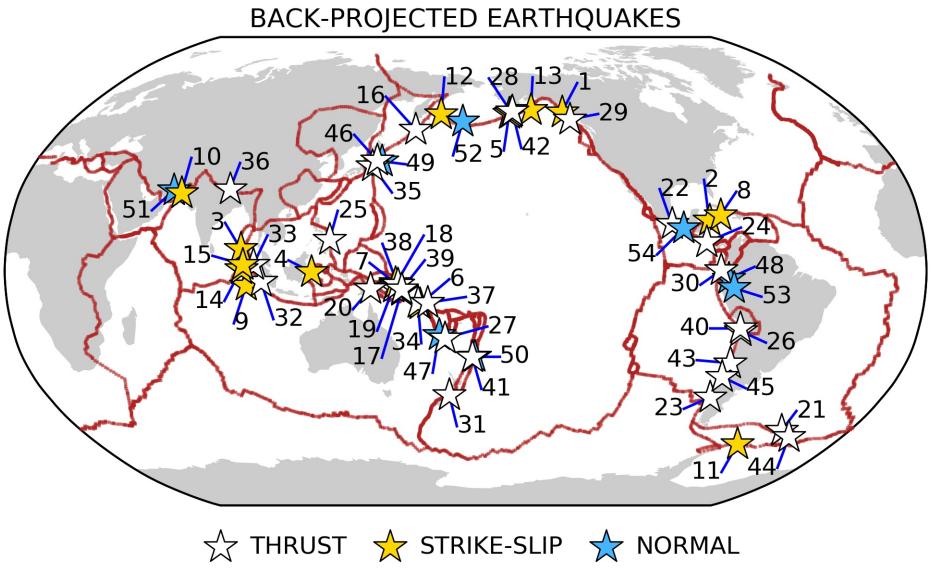

Figure 2. Global distribution of back-projected earthquakes colored by focal mechanism. Labels designate the earthquake ID, with details given in Fig. 5 and Tables S1–S3. Red segments show major plate boundaries (Bird, 2003).

2.2 Processing details

Fifty-four large earthquakes in the time range 01/2010-10/2021 (all events with $M_W \geq 7.5$, depth$\leq$200 km according to Global CMT catalog, `https://www.globalcmt.org`) were back-projected using the multi-array multi-phase approach. Fig. 2 shows the distribution of these earthquakes color-coded by faulting type. Thrust earthquakes dominated (57%) the catalog, followed by strike-slip (28%), and normal (15%) faulting mechanisms. Tables S1, S2 and S3 in the supporting information present the earthquake source parameters for strike-slip, thrust, and normal faulting earthquakes, respectively.

The number of (ad-hoc) arrays weighted and combined in the analysis depended on their availability at epicentral distances between 30–100°, where the P waveforms are not subject to complications like triplications as observed at smaller distances. The array selection and weighing prioritize even azimuthal distribution, while as many arrays as possible are incorporated.

Dense arrays are formed depending on configuration and geometry of permanent broadband networks, e.g., North America (e.g., US: United States National Seismic Network; AK: Alaska Regional Network), Japan (NIED Hi-net Network), Europe (many national and global networks distributed by ORFEUS-EIDA; Strollo et al. (2021)), and Africa (e.g., AF: AfricaArray). Additionally, local and regional networks (often temporary deployments) are evaluated (e.g., data availability, waveform coherence) to form smaller aperture arrays and maximize the azimuthal coverage. The extent to which a good azimuthal distribution can be achieved therefore differs between the different regions, but also with the time and time gap after the event (as temporary network data are often only openly available a few years after the experiment). Earthquakes in Indonesia are favorably located to be imaged with several arrays, e.g., networks in Asia, Europe, Africa, Australia, and Antarctica. In contrast, earthquakes in northern and central Chile suffer from limited coverage, although still a somewhat reasonable azimuthal distribution can be achieved by combining networks

in North America, Africa, and Antarctica. For events in southernmost Chile, Australian networks supplement the coverage.

After downloading, the instrument response is removed from the waveforms. P arrival times are predicted based on the IASP91 velocity model (Kennett & Engdahl, 1991). Static corrections are determined by measuring the relative time shifts of first arrivals on bandpass-filtered (0.4–3.0 Hz) vertical velocity waveforms with the adaptive stacking method of Rawlinson and Kennett (2004) based on the first 15 s after the P-wave onset. This frequency band is a little wider than the band used for the back-projection (0.5–2.0 Hz) and optimizes coherence while enough high frequencies are retained for a precise alignment. We also removed anomalous traces that could impact the waveform stack during the adaptive stacking as part of the input quality control.

For non-subduction megathrust earthquakes, the target grid was placed on a plane at the hypocentral depth, with grid points every 5 km. For subduction megathrust earthquakes, the grid followed the depth variations of the SLAB1.0 model (Hayes et al., 2012). For bilateral ruptures, we additionally mapped semblance maxima over a pre-defined sub-region of the grid to probe secondary rupture patterns. After visual inspection, we examined bilateral ruptures for the 27 February 2010 Maule (M_W 8.8), 11 March 2011 Tohoku-Oki (M_W 9.1), and 17 July 2017 Komandorsky Islands (M_W 7.8) earthquakes. Similarly, for the

16 September 2015 Illapel (M_W 8.3) earthquake, we tracked simultaneous up-dip and down-dip emissions (relative to the main slip area) by introducing a separate grid for the up-dip area. Although the 12 August 2021 South of Sandwich Islands earthquake was reported as a doublet by several agencies, we simply processed it as a single event, using the GEOFON hypocenter of the first event for calibration.

The back-projection considered a time window W of 6 s, chosen to be three times the dominant period, moved forward in 1 s increments. Longer values for W would have over-smoothed the rupture image. The back-projection frequency band (0.5–2.0 Hz) corresponded to the highest range for which consistently sufficient waveform coherency for rupture imaging has been obtained in prior studies (e.g., Palo et al., 2014; Meng et al., 2015, 2016, 2018). Finally, the end of the rupture was determined manually; frequent reactivation of earlier peaks or scattered semblance maxima are indicators for the end of the rupture. The apparent source time function of radiated energy was also considered, as small values compared to its peak also indicate the end of the rupture.

2.3 Estimation of basic source parameters

We have fully automated the earthquake rupture length, directivity, and speed based on the obtained rupture image from semblance peaks. For estimating rupture length (see Fig. 1c), firstly, candidate lengths L are estimated by the projection of the semblance

maxima (blue-red circles in Fig. 1c) on lines passing through the epicenter (white star) for all azimuths 0–180° (magenta line and open black circles show the realization for a 70° azimuth). The maximum value of L over all azimuths is chosen as the rupture length (red line in the bottom left subplot in Fig. 1c). Directivity is measured similarly, with lines of all azimuths 0–180° pivoting through the epicenter. However, the quantity minimized here is the sum of the squares of the perpendicular distances of all semblance maxima to the line (i.e., average squared lengths of blue arrows in Fig. 1c, which are shown symbolically for a few semblance peaks only). For simple ruptures, the azimuths returned by the length and directivity measurements will be very similar, but the length estimate is controlled by the end points, whereas the directivity estimate is controlled by all points simultaneously. The ambiguity in the actual directivity is resolved by considering an imaginary line perpendicular to the rupture direction and passing through the epicenter; we then choose the directivity based on which side of this line more semblance maxima are found. Additionally, the aspect ratio of the rupture is defined by the quotient between the minimum and maximum length estimates.

To determine the rupture speed, we first calculate estimates of instantaneous rupture velocities by dividing the distance between the epicenter and a subsequent semblance peak by the time elapsed since the origin time, which really represents the average rupture velocity from nucleation to the current time step. The resulting time series is strongly affected by

location uncertainties for small distances and times but stabilizes quickly (see Fig. 1c). The time series of rupture velocities is smoothed within a 4 s wide smoothing window, and its peak value is then taken as the event rupture speed; maxima during the first unstable 10 s are ignored. Although strictly speaking, this estimate represents the maximum average velocity (where the average is taken over all preceding times), it represents a reasonable estimate for most ruptures. Based on theoretical considerations, for supershear ruptures on simple faults, supershear velocities are thought to be attained quickly and maintained until the end of the rupture (Das & Aki, 1977), such that they can be detected straightforwardly by this estimation procedure. Nevertheless, the estimated rupture velocities can be significantly lower than the peak rupture speeds obtained for complex ruptures with directional changes, particularly those with a slow start. For the 17 December 2016 Solomon Islands earthquake, instead of referring back to the epicenter for the whole rupture duration, we reset the reference point to an emission point later in the rupture.

3 Results

3.1 Example: 2020 Kuril Islands Earthquake

We introduce the presentation of our results using the 25 March 2020 East of Kuril Islands (M_W 7.5) earthquake as an example, see Fig. 3. The results for all earthquakes are presented in the supplementary material, Figures S2–S60, with a summary of derived

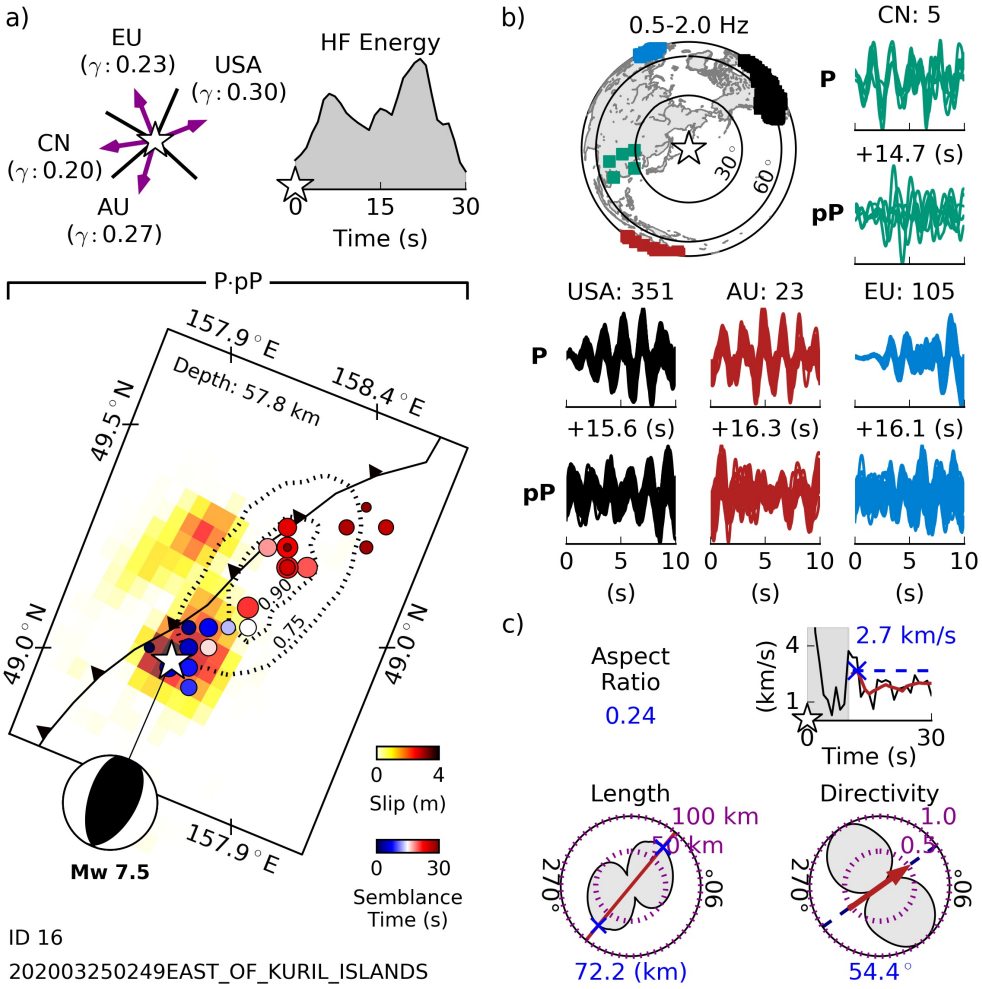

Figure 3. The 25 March 2020 East of Kuril Islands earthquake back-projection (0.5–2.0 Hz). a) Earthquake rupture image. Blue-red dots show semblance maxima tracking the earthquake rupture color-coded by time and scaled by energy radiated. Black dotted contours outline the short-period energy radiated (normalized to 1). The yellow-red polygons present the USGS-NEIC finite fault slip solution for comparison. Trench line derived from SLAB1.0 model (Hayes et al., 2012). Focal mechanism from Global CMT catalog. Inset: Array weights and energy radiated source time function. b) Multi-array configuration and time-shifted P and pP waveforms. c) Automatic rupture parameter determination; see Fig. 1c for further information on the format.

parameters in Fig. 5 and Table S4. We selected the Kuril Islands event because of the relatively simple rupture and because at the time of writing, to our knowledge, no other back-projection analysis had been published yet for this event. This event is an intraplate thrust earthquake, which probably was triggered by compressional bending stresses in the deep interior of the subducting Pacific plate (Ye et al., 2021).

The left inset of Fig. 3a shows the distribution of arrays, where the arrays in North America and Australia are weighted more strongly as they cover a larger backazimuthal range. In Fig. 3b the waveform coherency near the rupture initiation is visualized. It is generally good except for the pP phase at the China array. The main plot compares the back-projected rupture with the USGS-NEIC finite fault slip solution (`https://earthquake.usgs.gov/earthquakes/eventpage/us70008fi4/finite-fault`); for other events, frequently finite slip models from the literature are shown instead. Because this event is not a subduction megathrust earthquake, we back-projected onto a horizontal plane at 58 km depth, the hypocentral depth of the event. While in theory, it might be desirable to use the focal mechanism to define an inclined plane for back-projection, in practice, it is not easy to determine which nodal plane is the fault plane, except for megathrust events. For the East of Kuril Islands earthquake, the USGS-NEIC finite fault solution preferred the south-east dipping plane, whereas the finite fault solution of Ye et al. (2021) favored the northwest-dipping fault plane. A further advantage of a horizontal plane is that this

assumption will not fail in case of more than one planar fault being activated (e.g., 2018 Gulf of Alaska earthquake; Fig. S45). For the Kuril event, the main slip patch appeared close to the epicenter, and at the beginning of the rupture, both finite slip and short-period rupture spatially agreed. After 15 s, the high-frequency rupture propagated to the east of the secondary slip patch. This time period revealed the most energetic short-period emission. Close to this area, the most intense aftershock activity was observed (see Fig. 1 of Ye et al., 2021). The final high-frequency emissions occurred even further to the east-northeast, apparently far from the finite-slip area, but also here aftershocks occurred nearby.

The rupture propagated unilaterally in a linear manner, making the length and directivity estimation unambiguous (Fig. 3c). The implied strike direction of the rupture track is clockwise rotated by some 10–20° with respect to the strike direction indicated by the moment tensor. At face value, this would imply that the short-period emission points did not strictly propagate along strike but moved additionally up-dip (or down-dip, depending on which fault plane is the correct one).

We can compare the time history of emitted short-period energy for the Kuril Islands earthquake with the moment rate obtained from the USGS finite slip solution (highlighted in Fig. 4). Both show two peaks, and the timing of the first peak and subsequent trough agree. However, at short periods, the second peak of energy exceeded the first one, and the

rupture appeared to continue for longer. Interestingly, in the source time function estimated by Ye et al. (2021) (their Fig. 1), the moment rate of the second peak also exceeded the first one.

3.2 Short-period source time functions

The short-period energy time functions for all events are compared with USGS and SCARDEC (Vallée & Doeut, 2016) moment rates in Fig. 4. The time history of radiated high-frequency seismic energy frequently agree (e.g., 2021 Chignik, ID 42; 2020 Caribbean, ID 8; 2016 Kaikoura, ID 31; 2013 Scotia Sea, ID 11; 2012 Wharton Basin, ID 15; 2010 Mentawai, ID 32) with the seismic moment rate functions, but it is sometimes apparently time-shifted, following (e.g., 2016 Melinka, ID 23; 2013 Craig, ID 1; 2011 Tohoku-Oki, ID 46) or, less often, preceding (e.g., 2016 Solomon, ID 34; 2012 Philippine Islands, ID 25) the seismic moment rate. A few earthquakes presented a quite different shape (e.g., 2014 Iquique-Pisagua, ID 40; 2019 Northern Peru, ID 53). However, it has to be noted that the USGS and SCARDEC moment rates also do not always agree. One example is the M_W 8.1 Iquique-Pisagua earthquake (ID 40; Fig. 4), where the SCARDEC estimate suggested a much shorter source time function. For the M_W 8.2 Chiapas earthquake (ID 54; Fig. 4), SCARDEC (and the short-period energy function) completely lack a secondary peak seen in the USGS estimate. Because of this variety, it is difficult to judge whether the differences

between moment rate and short-period energy function are physical, i.e., relate to the time-varying ratio of slip to high energy emissions, methodological artifacts, or both. A possible physical explanation is that the ratio of short-period to long-period spectral energy is known to vary significantly between earthquakes (or equivalently, the seismic energy to moment relation, which is related to the variability in stress drop). It seems likely that this variability can also extend to the case of different asperities within a given rupture, which would then cause different time histories of moment rate function and short-period energy function.

3.3 Subduction zone megathrust ruptures

We now consider the rupture patterns of subduction megathrust earthquakes, specifically the spatial relationship between finite-slip models of rupture displacement and short period emissions. As mentioned, previous observations of short-period ruptures indicated a strong preference for emissions down-dip of the main slip asperity (e.g., Lay et al., 2012). Fig. 6 summarizes the rupture patterns for the largest subduction zone megathrust events in our catalog. We can distinguish a variety of typical patterns referred to as down-dip, (down-dip, up-dip, or double-)encircling, and segmented, defined by the relation of short-period radiation and the main asperity (see Fig. 6 inset on the bottom right, for a graphical definition; and supporting Movie S1).

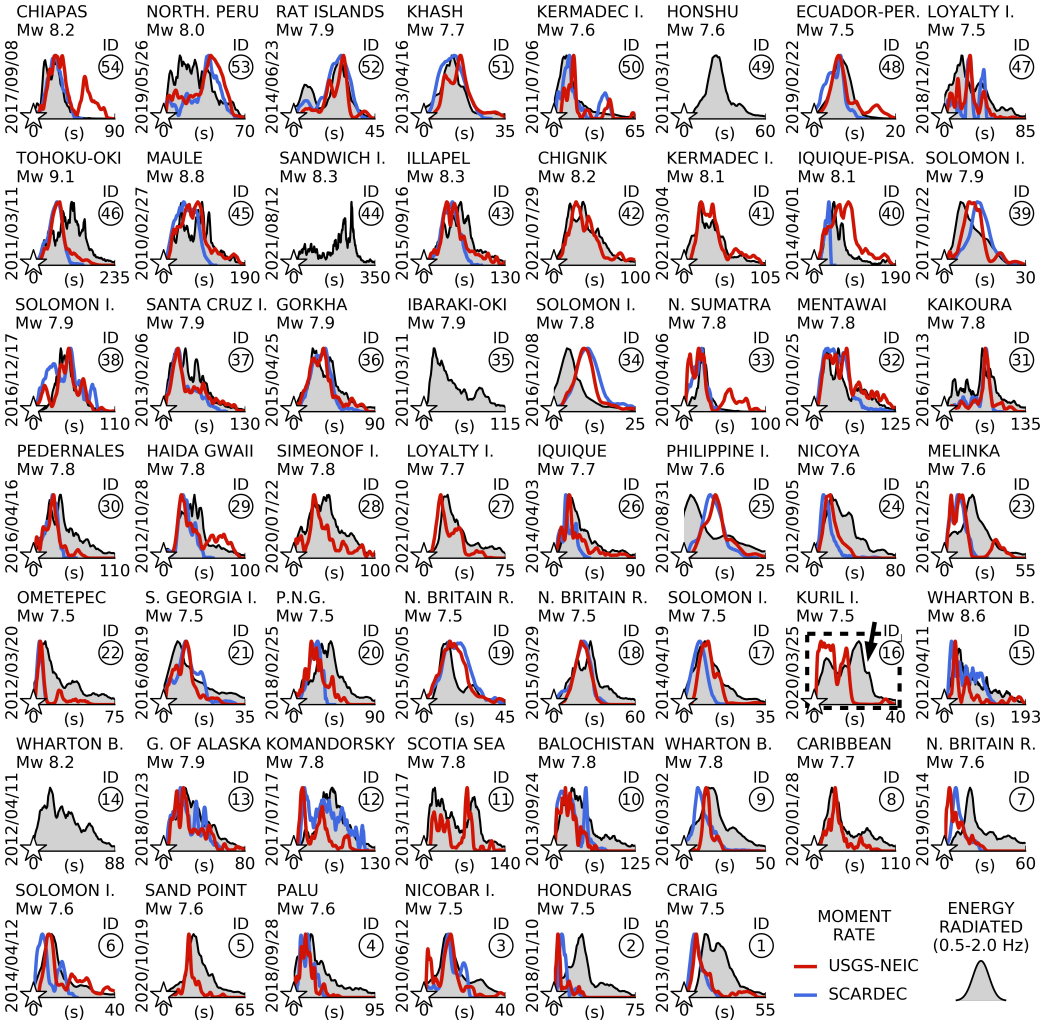

Figure 4. Short-period (0.5–2.0 Hz) energy radiated source time functions derived from back-projection. The energy radiated maxima evaluated over the rupture time provides the source time function (in gray). Additionally, USGS-NEIC (in red) and SCARDEC (in blue) moment rate functions are shown for comparison. The event highlighted with a dashed box is used as an example and discussed in detail in the text.

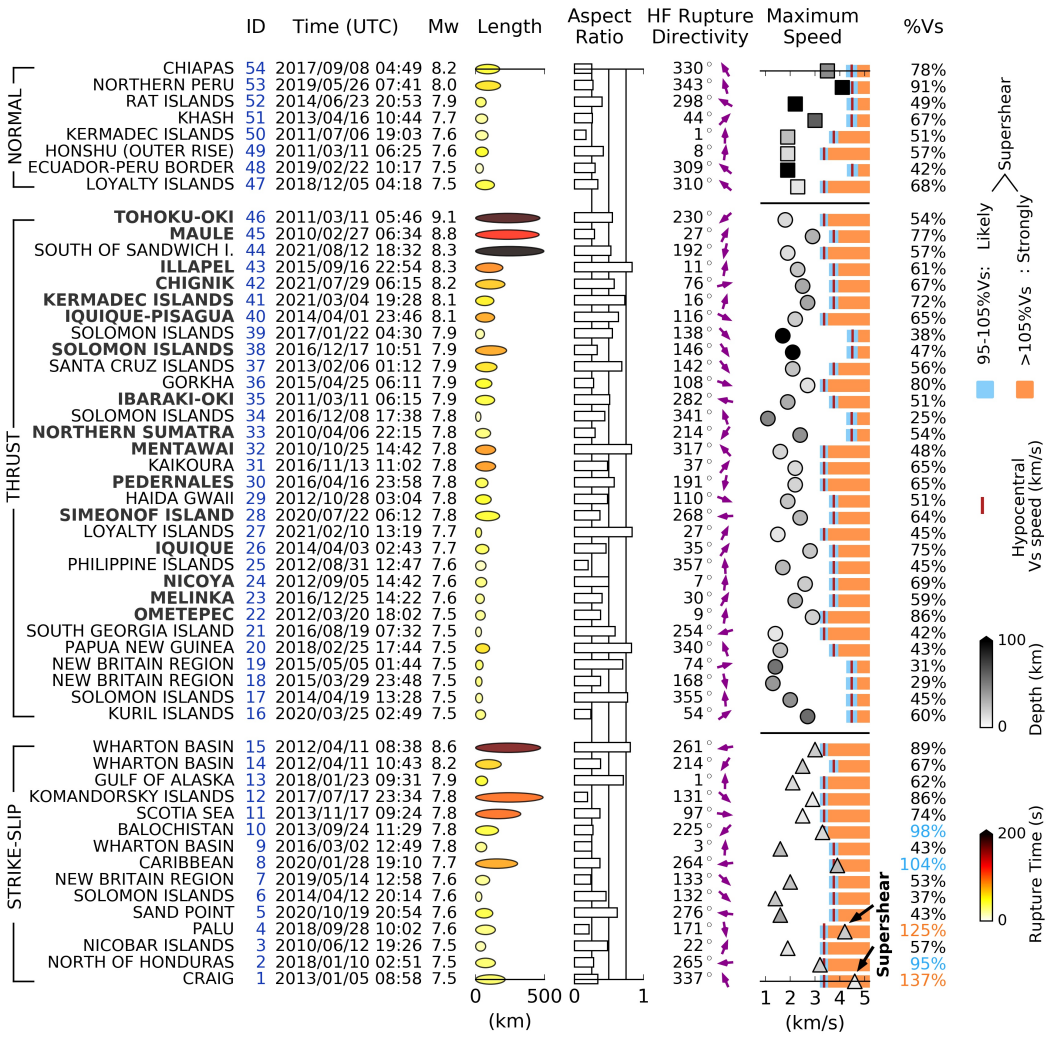

Figure 5. Earthquake rupture parameters from back-projection (0.5–2.0 Hz). Event ID (for cross-referencing to other figures, tables, and supporting information), moment magnitude, rupture length (colored by rupture time), aspect ratio, directivity, and rupture speed (colored by hypocentral depth). The events are categorized into normal (upper), thrust (middle), and strike-slip (bottom) earthquakes, with the order in each category determined by magnitude. Events in bold text are assumed to be subduction megathrust earthquakes. The vertical red bars in the rupture speed panel show the expected shear wave speed (V_S) at the hypocentral depth in the IASP91 velocity model (Kennett & Engdahl, 1991). Ruptures in the range 95–105%V_S and >105%V_S define 'likely' and 'strongly' supershear earthquakes, respectively.

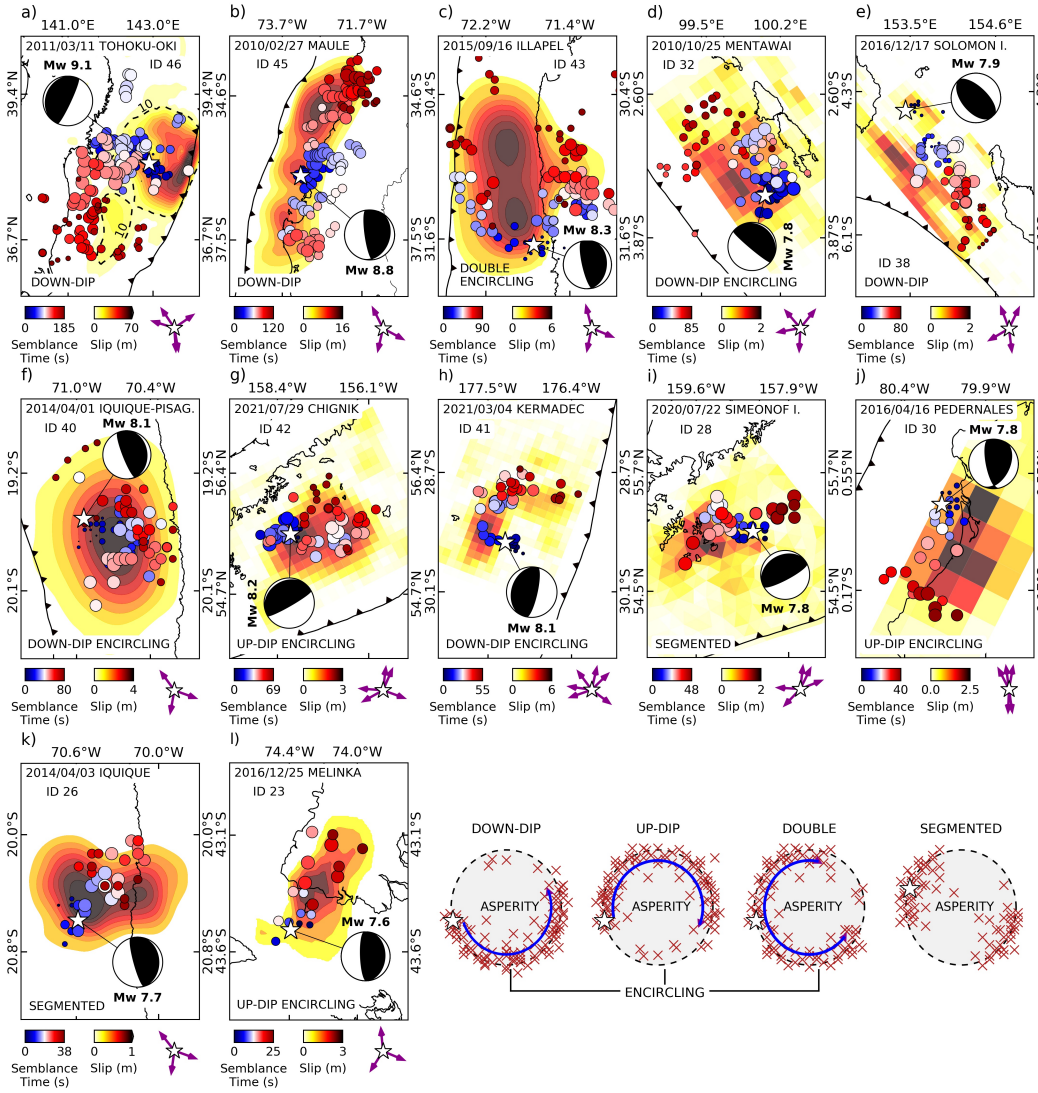

Figure 6. Back-projected earthquake rupture patterns (0.5–2.0 Hz) for major subduction zone megathrust earthquakes. Blue-red dots show semblance maxima tracking the earthquake rupture color-coded by time and scaled by energy radiated. The subplots are sorted by rupture duration. The dark-magenta arrows (lower-right corner) indicate the multi-array distribution relative to the epicenter (white star). Trench location from SLAB1.0 model (Hayes et al., 2012); focal mechanisms from Global CMT catalog. The yellow-red background shows the slip distribution of a) Iinuma et al. (2012), b) Moreno et al. (2012) c) Tilmann et al. (2016), d), e), g) and h) USGS-NEIC finite fault solution, f) and k) Schurr et al. (2014), i) Crowell and Melgar (2020), j) Heidarzadeh et al. (2017), and l) Moreno et al. (2018). Bottom inset: Canonical high-frequency rupture patterns. The dominant type is noted in the bottom of each plot.

The 2010 Maule earthquake showed a classical down-dip rupture with a bilateral propagation (∼29% southward; Fig. 6b and S2). The 2011 Tohoku-Oki earthquake also ruptured bilaterally and mainly down-dip (Fig. 6a and S7). However, we draw attention to the rupture near the trench where large shallow slip occurred (up to 50 m). In the last phase of the rupture (135–180 s), a subsidiary pattern with up-dip and down-dip emissions encircling the second larger slip area off the coast of Fukushima Prefecture can be discerned (see the southern 10 m contour in Fig. 6a).

Rupture images were not always limited to only the deeper portion of the megathrust. The observations included several short-period ruptures showing encircling patterns (see inset in Fig. 6), as previously only clearly reported for the 2016 Illapel earthquake. The 2021 Kermadec Islands earthquake first propagated to the northeast and down-dip of the main asperity, followed by a circular shape with the rupture moving up-dip in the final phase (Fig. 6h and S58). Similarly, the 2010 Mentawai earthquake first propagated along the down-dip edge of the main asperity and then ruptured up-dip to the near trench region (Fig. 6d and S6). The 2014 Iquique-Pisagua earthquake ruptured with a half-ellipse pattern surrounding the larger slip area (Fig. 6f and S22). For the 2016 Pedernales earthquake, the reverse of the conventional pattern occurred, with short periods being radiated up-dip of the main asperity, followed by a down-dip propagation near the southern tip of the rupture (Fig. 6j and S33); a similar sequence defined the 2016 Melinka earthquake rupture (Fig. 6l

and S39). The 2021 Chignik earthquake (Fig. 6g and S59) showed an eastward propagation that fully encircled the slip area, but up-dip emissions dominated the rupture. More or less parallel and contemporaneous rupture 'tracks' up-dip and down-dip of the main asperity were observed for the 2015 Illapel earthquake in central Chile (Fig. 6c and S31), as also pointed out by the dedicated back-projection study of Meng et al. (2018) for this event. The main rupture propagated northward along the down-dip. A secondary front in the shallow part of the megathrust (less than ∼15 km depth) followed the region parallel to the trench for over ∼150 km, completing a double encircling pattern.

Other observations exhibited segmented ruptures, with short-period emissions concentrated on asperity edges. The 2014 Iquique event showed a unilateral northeast short-period rupture partitioned around the asperity but outlining the maximum slip region (Fig. 6k and Fig. S23). Offshore of the Alaska Peninsula, the 2020 Simeonof Island earthquake first propagated down-dip to the northwest and west (Fig. 6i and S55), but the last emissions originated east of the epicenter.

The 2021 South of Sandwich Islands earthquake doublet, the most recent event in our catalog, is another complex rupture (Fig. 7 and S60). Although major agencies all identified the earthquake as a doublet, estimates of the partitioning of moment between the sub-events and the onset of second sub-event differ considerably, including large discrepancies in the

estimated total moment (GCMT: M_W 8.3 and 7.9 for the first and second sub-event, origin times separated by 178 s; GEOFON: M_W 7.7 and 8.0, +153 s; USGS: M_W 7.5 and 8.1, +148 s). The event showed a predominantly SW rupture propagation with an initial short phase of NW-directed propagation. For about 200 s, the rupture followed the megathrust bend formed by the subducting South American Plate and the overriding Sandwich Plate. At the southern edge of the rupture, final emissions (up to 300 s) occurred near the transform fault margin where the Sandwich Plate borders the Antarctic Plate. However, uncertainties in short-period emission points are too large to unambiguously apportion slip to either the transform section or the subduction megathrust.

The resulting inferred rupture length of 496 km covered nearly three-quarters of the South Sandwich subduction zone, and is at least twice as long as expected for earthquakes of this magnitude based on scaling relations by Wells and Coppersmith (1994) and Blaser et al. (2010), see section 3.5 for quantitative analysis of short-period rupture lengths. The radiated short-period energy function is clearly separated into two phases (top inset in Fig. 7), presumably corresponding to the two sub-events; the origin time of the second sub-event in the GEOFON and USGS split coincides approximately with the minimum of the short-period energy function between the two peaks, and the second peak is clearly larger, in qualitative agreement with the relative moment sizes of the two sub-events in these catalogs. Additionally, Fig. 7 compares the back-projected rupture with a month of

cumulative seismicity after the first event. The short-period rupture followed mainly the down-dip band of seismicity, while a burst of emissions east of the epicenter outlined the area close to the trench, adjacent to a patch of outer-rise aftershocks.

In order to evaluate the depth distribution of seismic radiation more systematically, Fig. 8 presents the depth distribution of radiated short-period energy (more specifically, the maximum energy per depth level, normalized for each event). We remind the reader that depth is not resolved explicitly, but the horizontal position is translated to depth, assuming slip occurs on the slab interface defined by the SLAB1.0 model. The maximum energy distribution occurred between 15 and 45 km depth, with all depths in between represented fairly evenly but a higher concentration at depths larger than 25 km, as visible in the slope break in the figure. The resulting median depth is ∼30 km, which is close to the typical depth of the transition between domains B and C of Lay et al. (2012), i.e., down-dip of the main asperity, but the large variation also demonstrated that the pattern of dominant down-dip high-frequency radiation has many exceptions. Also, events with maximum radiation at similar depths do not necessarily share the same characteristics. For example, the 2010 Mentawai, 2012 Ometepec, and 2016 Pedernales earthquakes all showed dominant radiation in the shallow part of the megathrust ($<$ 25 km depth). But the 2010 Mentawai event was a tsunamigenic earthquake with an unusually shallow main asperity, therefore, this shallow depth still corresponds to dominant radiation down-dip or down-dip

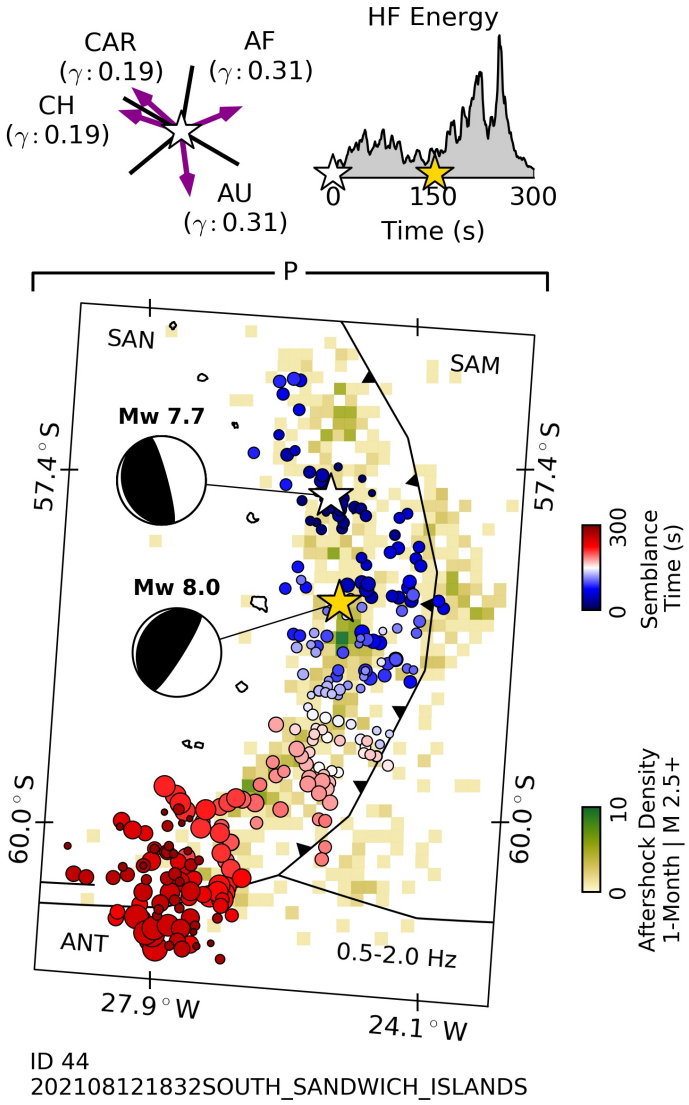

Figure 7. The 2021 South of Sandwich Islands earthquake back-projection (0.5–2.0 Hz). Blue-red dots show semblance maxima tracking the earthquake rupture color-coded by time and scaled by energy radiated. The earthquake is a composite event, with the white and yellow star representing the (GFZ) epicenters and origin times of the two sub-events. Focal mechanisms are from the GEOFON (GFZ) moment tensor catalog. The yellow-green polygons present a month of cumulative seismicity (M 2.5+; USGS-NEIC) (patches of 10 × 10 km; M 2.5+ from the USGS-NEIC earthquake catalog; `https://earthquake.usgs.gov/earthquakes/search/`). Trench distribution from Styron and Pagani (2020). Tectonic setting: South American (SAM), Sandwich (SAN), and Antarctic (ANT) plates. Inset: Array weights and energy radiated source time function.

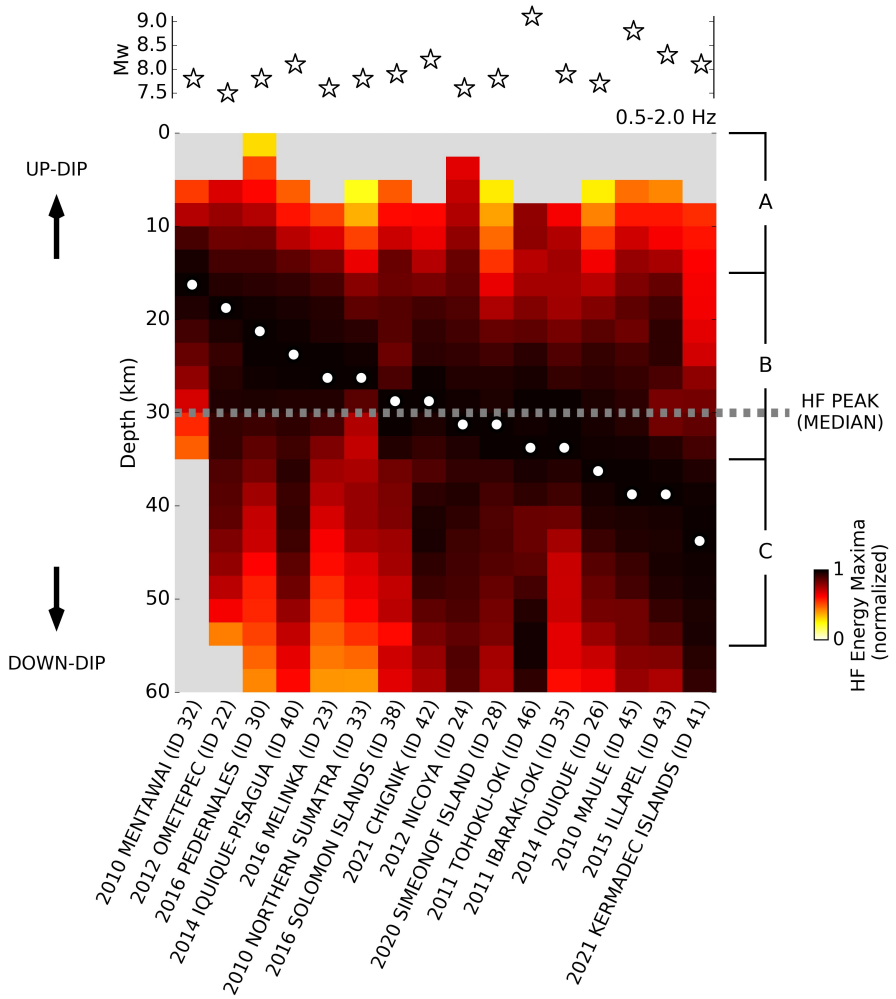

Figure 8. Depth distribution of radiated short-period energy (0.5–2.0 Hz) for all megathrust earthquakes. The maximum back-projected energy is extracted and displayed for each depth, normalized to 1 separately for each earthquake (yellow-red shading). White dots mark the depths for the peak values, showing the depth at which most short-period energy was emitted. The gray dashed line presents the median depth for short-period emissions. Gray polygons show areas with no data, i.e., depths, which were not included in the search grid for the respective earthquake. Inset: Earthquake magnitude (upper) and indicative depths of A-B-C megathrust faulting domains (right) following the definition of Lay et al. (2012); actual depths will differ somewhat between subduction zones.

encircling pattern. In contrast, the main rupture asperities for the 2016 Pedernales and 2012 Ometepec earthquakes were in domain B or even C, such that the strong shallow short-period emissions indicated an up-dip or up-dip encircling patterns. Most of the great subduction earthquakes with $M_W > 8.0$, e.g., 2010 Maule, 2011 Tohoku-Oki, 2015 Illapel, 2021 Kermadec Islands, and 2021 Chignik earthquakes, radiated predominantly in deeper regions at 30–45 km depth, consistent with the classic down-dip segmentation described by Lay et al. (2012).

3.4 Earthquake rupture speeds

Fig. 5 shows the speed estimations, additionally expressed as a percentage of the shear velocity at the hypocentral depth in the IASP91 model. The underlying rupture speed time series are summarized in Fig. S1. Because the rupture speed estimates are based on the horizontal projection, rupture velocity might be underestimated if rupturing up-dip or down-dip dipping faults, e.g., for a dip angle of 30° this effect would amount to ∼15%. However, this effect will only affect a small subset of intra-plate thrust or normal faults.

Thrust earthquakes averaged a rupture propagation speed of 2.1 km/s and 56% of the shear wave speed, with a range between 25% and 86% of the shear wave speed, which places propagation speeds firmly in the expected sub-Rayleigh regime. The 2010 Mentawai, 2011 Tohoku-Oki, and 2021 South of Sandwich Islands earthquakes were slower than the average.

The Mentawai and Tohoku-Oki events are characterized by large displacement at very shallow depths, implying a low normal stress environment and large tsunamis. The outer-rise seismicity and notable near trench short-period rupture emissions for the Sandwich Islands event could also indicate a shallower rupture for at least part of the rupture propagation. However, finite fault modeling results are required for an extended interpretation.

A special case is presented by the 17 December 2016 Solomon Islands earthquake (Fig. 6e and S37). A megathrust rupture released the bulk of the moment, but its hypocenter is at 105 km depth, and the first motion mechanism indicated down-dip intraslab faulting, which is thought to have triggered the main megathrust event (e.g., Lay et al., 2017; Lee et al., 2018). In the rupture image, this sequence was visible as a gap of ∼55 km between the first emissions and the dominant megathrust pattern, which also outlined a southeast propagation of the rupture along the strike of the megathrust. The short time interval needed to cross the gap implied an extremely fast rupture speed of 5.7 km/s equivalent to ∼71% of the P wave speed at the hypocentral depth, indicating that most likely P waves from the intraslab sub-event triggered the megathrust rupture (note that the relative P wave speed is calculated in the reference model; P wave speeds in the down-going oceanic crust would be slower, thus higher percentages are possible). To explore rupture propagation in the main phase, we therefore placed the reference point at the megathrust rupture initiation; then, a more typical rupture propagation speed of 2.1 km/s was obtained (Fig. S38).

For normal earthquakes, the average was 2.6 km/s and 63% of the shear wave speed, with a range between 42% and 91% of the shear wave speed. The 2019 Northern Peru (106 km depth; Fig. S51) earthquake showed the fastest rupture (4.1 km/s and 91%V_s), which is at the upper limit of the sub-Rayleigh speed. Although this intermediate-depth event was fast, the depth does not seem to have a systematic effect on rupture velocity. For example, the 2014 Rat Islands event at nearly the same depth (109 km; Fig. S27) and 2019 Ecuador-Peru Border Region earthquake (at 146 km depth; Fig. S49) ruptured comparably slowly at 2.2 and 1.9 km/s. For the Rat Island event, previous back projections and finite fault modeling showed a similar rupture velocity in the range of ∼1.5–2.5 km/s (e.g., Ye et al., 2014; Twardzik & Ji, 2015). However, the lack of solid evidence for a shallow or steeply-dipping fault plane preference makes the projection effects in the rupture velocity difficult to evaluate.

Strike-slip earthquakes showed the greatest variability. The average rupture speed was 2.7 km/s and 78% of the shear wave speed, but the range spans from 37% to 137% of the shear wave speed. Two events were clearly within the unstable supershear range (between V_s and $\sqrt{2}V_s$): the 2013 Craig (4.6 km/s and 137%V_s; Fig. S17) and 2018 Palu (4.2 km/s and 125%V_s; Fig. S47) earthquakes. The Palu event was supershear from early on as reported also by Bao et al. (2019) using the high-resolution MUSIC back-projection method, while the oceanic interplate Craig initiated at subshear speed and transitioned to supershear

after ∼20 s (see time series and supershear reference in Fig. S1). The average rupture speed for the Craig earthquake inferred by us agrees with the finite-fault modeling results (4–5 km/s) of Aderhold and Abercrombie (2015). Previously, Yue et al. (2013) provided faster peak velocity estimates from Sg and Sn arrivals (> 4.5 km/s) and finite-fault inversion (5.5–6 km/s), but as we do not consider time-variable propagation rates, these observations are not in conflict. The 2013 Balochistan event propagated at a speed of 3.3 km/s (Fig. S20), representing 98% of the shear wave speed, that is, around the shear velocity but (very likely) faster than Rayleigh waves. Additionally, the 2018 North of Honduras (95%V_s; Fig. S44) and 2020 Caribbean (104%V_s; Fig. S53) earthquakes propagated at 'likely' supershear (95–105%V_s; by assuming expected rupture velocity errors in the estimates). For the Caribbean earthquake, Tadapansawut et al. (2021) inferred supershear rupture fronts with peak velocities larger than 5 km/s from finite-fault modeling, i.e., significantly faster than our average-based estimates.

Errors in emission point location arise from the array configuration and frequency band and can affect high-frequency rupture speed estimates, while finite-fault modeling operates at relatively low frequencies with imposed conditions, i.e., imposed speed boundaries and fault geometry. Marty et al. (2019) showed that rupture fronts derived from short-period backprojections propagate close to the rupture speed in laboratory experiments. It is an open question whether differences in rupture speed between back-projection and finite-

fault modeling seen here might be related to methodological concerns or reflect the more heterogeneous nature of natural fault systems.

3.5 Rupture length and aspect ratio estimates

The earthquake rupture length estimates are used to determine magnitude-length scaling relations for each faulting slip type (normal, thrust, and strike-slip). The logarithm of rupture length and moment magnitude controlled the regression coefficients for the back-projected scaling relations (Fig. 9 and supporting Table S5). Due to the composite nature of the earthquake and variability in moment estimates, the Sandwich Islands event was not included in the regression for thrust magnitude-length scaling relation.

Thrust and normal earthquakes showed similar magnitude-length dependencies, while strike-slip earthquakes had a large data dispersion on average. Fig. 5 shows a comparative view of the rupture lengths colored by rupture time and sorted by moment magnitude for normal (upper), thrust (middle), and strike-slip (bottom) earthquakes.

We further explored the relationship between aspect ratio and complexity. Simple elongated ruptures generally are characterized by small aspect ratios, e.g., the 2017 Komandorsky Islands (ratio ~ 0.19; Fig. S41), 2016 Wharton Basin (ratio ~ 0.25; Fig. S32), and 2011 Kermadec Islands (ratio ~ 0.17; Fig. S10) earthquakes, all of them bilateral ruptures. In contrast, complex events with no straightforward interpretation of 'rupture length' tend

to have large values. For strike-slip events, events with aspect ratio close to 1 often indicate the rupture of multiple faults. Prominent examples are the 2012 Wharton Basin (ratio $\sim$ 0.81; Fig. S12) and 2018 Gulf of Alaska (ratio $\sim$ 0.71; Fig. S45) earthquakes that ruptured a conjugate fault system. For the 2020 Sand Point strike-slip event, Santellanes et al. (2021) proposed that considerable slip occurred on the megathrust; the back-projection showed northward and eastward complex rupture emissions, but mostly eastward nearly along the megathrust strike (ratio $\sim$ 0.62; Fig. S56), which is relatively westward and up-dip of the 2020 Simeonof megathrust rupture (Fig. S55). For thrust earthquakes, the aspect ratio also quantified complexity, but the complexity usually does not arise from a rupture on different faults, but from the distribution of high-frequency on the megathrust, e.g., the 2015 Illapel earthquake and its double encircling pattern (ratio $\sim$ 0.84; Fig. S31). However, regardless of the faulting slip type, a compact rupture can also result in an aspect ratio close to 1 due to the greater importance of scatter for smaller ruptures, e.g., the 2021 Loyalty Islands (ratio $\sim$ 0.84; Fig. S57) and 2014 Solomon Islands (ratio $\sim$ 0.77; Fig. S25) earthquakes. Therefore, rupture complexity is linked to aspect ratios $>\sim$ 0.5, but such a larger value does not necessarily imply complexity but can also indicate compactness, particularly for earthquakes with $M_W <\sim 8$. Finally, we note that aspect ratios are always evaluated in the horizontal plane, implying that results for strongly dipping faults might not be directly comparable.

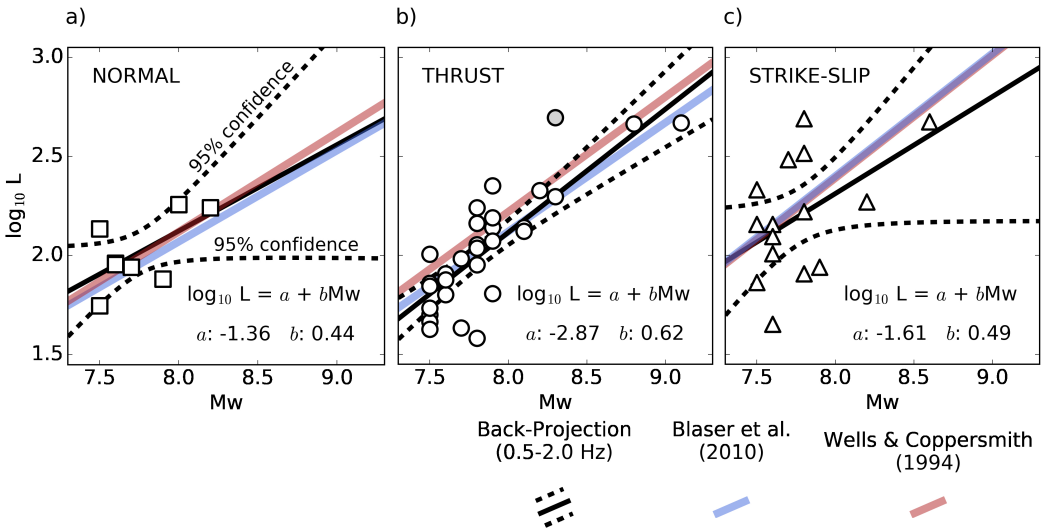

Figure 9. Rupture length scaling relations for short-period back-projection based estimates. a) Normal, b) thrust and c) strike-slip earthquakes. The black line shows the back-projection relationships (solid line) and the 95% of confidence interval predicted (dashed line). The squares, circles, and triangles present the data distribution for each faulting type. The gray circle shows the 2021 South of Sandwich Islands earthquake not included in the regression. Blue and red lines show the well-known scaling relationships of Blaser et al. (2010) and Wells and Coppersmith (1994) for comparison.

4 Discussion

4.1 Multi-array multi-phase imaging method

A multi-array configuration provides wide coverage in azimuth with benefits in resolvability, but a heterogeneous distribution can promote biases, e.g., 'swimming' artifacts. As an example, we consider the 19 April 2014 Solomon Islands earthquake (M_W 7.5; 43 km depth): the multi-array back-projection with the inclusion of the depth phase approach showed a short-period rupture outlining the finite fault slip model (see Fig. S25). However, the rupture differed significantly when the arrays were restricted in number, azimuthal distribution, or depth phases were not considered (Fig. S26). For example, P wave backprojections from one or two arrays showed a significant time-space trade-off of the earthquake rupture in the form of swimming artifacts, e.g., a drift towards the arrays in Alaska and Japan (Fig. S26a–b). These artifacts are progressively reduced with more and well-distributed arrays (Fig. S26c–d). If depth phases are incorporated, the same array coverage offered a moderate reduction of artifacts (Fig. S26e–h). This is also noticeable for the source time function, which is strongly affected by depth phases when the arrays are poorly distributed, and only P waveforms are included. The depth phase appears as a spurious secondary peak at ∼15 s (see inset in Fig. S26a–c).

Further detailed analyses of the effects of artificially restricted coverage are shown in the supplementary material for selected events and exhibit similar effects: the 2010 Northern Sumatra (Fig. S4), 2017 Chiapas (Fig. S43), 2019 Northern Peru (Fig. S52), and 2020 East of Kuril Islands (Fig. S54) earthquakes.

4.2 Complex megathrust ruptures and depth-varying short-period radiation

Seismicity prior to a great earthquake is often demonstrated to be active on the rupture zone edge while a seismic quiescence dominates the region later experiencing the maximum slip according to the 'Mogi doughnut' hypothesis (e.g., Mogi, 1969; Kelleher & Savino, 1975). According to this hypothesis, the spots at the asperity edge become seismically active as the stress on the asperity increases, outlining the potential rupture area (e.g., Kanamori, 1981). For example, Schurr et al. (2020) observed a Mogi doughnut in the years prior to the 2014 Iquique-Pisagua earthquake. Sippl et al. (2020) showed microseismicity forming three half-ellipses along the central Chile megathrust, with one of them encircling the 2015 Illapel earthquake area. In back-projection, short-period ruptures are related to stress conditions and rupture velocity variations (e.g., Marty et al., 2019). Therefore, back-projected rupture patterns might likewise be an indication of the high-stress gradient around the asperity, equivalently to the Mogi doughnut pattern of seismicity.

598 Many megathrust earthquakes exhibited encircling patterns, where the back-projection
599 highlights propagation to shallower regions. This pattern could be related to the presence of
600 seismogenic barriers under the assumption of a strong rupture deceleration or stopping phase
601 (e.g., Madariaga, 1983). The 2015 Illapel earthquake showed a double encircling pattern; it
602 was first observed by Meng et al. (2018) using the high-resolution MUSIC back-projection
603 method and interpreted as a splitting of rupture fronts surrounding a large asperity or
604 barrier. The 2021 Chignik earthquake is another example of a rupture forming a ring
605 around the slip patch with both up-dip and down-dip limits included. The 2010 Mentawai
606 and 2011 Tohoku-Oki earthquakes were tsunamigenic with a rupture that propagated up to
607 the trench (e.g., Lay et al., 2011; Hill et al., 2012; Iinuma et al., 2012). This is compatible
608 with the back-projected rupture, where semblance peaks are (unusually) partly located at
609 shallow regions below accretionary structures. The transition from the seismogenic to a
610 shallow aseismic sliding region might explain a strong rupture velocity variation and the
611 shallow source of short-period radiation. For the 2016 Pedernales event, Agurto-Detzel et
612 al. (2019) proposed, in the up-dip limit of the earthquake rupture, a barrier mechanically
613 controlled by the subduction of a rough oceanic relief. Similarly, the back-projection revealed
614 a rupture up-dip of the slip distribution (at 15–20 km depth; Fig. S33) that agrees with high
615 residual ($>\sim$ 1 km) bathymetry data (see Fig. 9 of Agurto-Detzel et al., 2019), indicating a

first-order relationship between the along-dip barrier structure and short-period earthquake radiation.

In summary, short-period energy maxima emitted from the shallow part of the megathrust (< 35 km depth; A and B regions) resulted in being more frequent than suggested by earlier results. The 2010 Mentawai, 2012 Ometepec, and 2016 Pedernales earthquakes emitted their maximum short-period radiation from very shallow regions (< 25 km depth), unlike in the classic Lay et al. (2012) dip-segmentation. The median depth for the energy radiated peak falls at the end of domain B (15–35 km; Fig. 8) of Lay et al. (2012), that is, before the transition from regions with modest to high amounts of coherent short-period energy, but, as we have seen, large deviations are not uncommon between large subduction earthquakes.

4.3 Rupture length scaling relations at short periods

We compare the newly derived short-period scaling relation to established scaling relations (e.g., Wells & Coppersmith, 1994; Blaser et al., 2010) which were derived from large data sets using rupture lengths estimated from aftershocks sequences, geodetic modeling, and empirical relationships (Fig. 9, Table S5). For normal faulting earthquakes, our scaling relation is very similar to those derived from both Wells and Coppersmith (1994) and Blaser et al. (2010) (Fig. 9a). For thrust earthquakes, our scaling relation predicts shorter thrust

rupture lengths (Fig. 9b) than Wells and Coppersmith (1994) but is close to the predictions of Blaser et al. (2010) (which is the newer reference based on a larger database). Lengths for strike-slip earthquakes presented a large dispersion (Fig. 9c), providing estimates generally shorter than Blaser et al. (2010) and Wells and Coppersmith (1994) but still within the expected, albeit large, uncertainty. A first limitation here is the sparsity of strike-slip events with $M_W > \sim 8$. Second, several of the large strike-slip earthquakes were complex events rupturing multiple conjugate faults, leading to large ambiguity in the interpretation of the rupture length determined by our algorithm, as the cumulative fault length ruptured will be much larger than this estimate. This pattern is often found for intraplate earthquakes in the oceanic lithosphere, for example, the great 2012 Wharton Basin (e.g., Meng et al., 2012a; Duputel et al., 2012; Satriano et al., 2012; Hill et al., 2015) and 2018 Gulf of Alaska (e.g., Lay et al., 2018; Krabbenhoeft et al., 2018; Ruppert et al., 2018) earthquakes, where the back-projection results are broadly compatible with the more comprehensive assessments carried out in these references, which also included aftershocks, seafloor topography and/or finite fault modeling in the analysis.

5 Conclusions

We presented a catalog of short-period rupture histories for 54 large earthquakes (0.5–2.0 Hz; $M_W \geq 7.5$; 01/2010-10/2021) based on a new implementation of the teleseismic

back-projection method, which takes into account multiple arrays and combined P and pP waveforms (for earthquakes deeper than 40 km). Based on the back-projection results, rupture length, directivity, rupture speed, and aspect ratio are estimated algorithmically. The main findings are as follows:

1. We find distinct differences in rupture patterns between finite fault slip models and short-period emissions for subduction megathrust earthquakes. We confirm a preference for short-period seismic energy to be emitted down-dip of the main slip asperity (as previously reported in the literature), but additionally identify many examples of segmented and encircling configurations with down-dip, up-dip, or double patterns outlining coseismic slip patches.
2. Short-period rupture patterns for megathrust earthquakes, e.g., encircling patterns around slip patches, might result from the stress gradient around asperities (including along-strike seismogenic barriers).
3. Earthquake rupture speeds were consistently in the sub-Rayleigh regime for thrust and normal faulting earthquakes, with a median of 56% and 63% of the shear wave speed, respectively. Strike-slip earthquakes showed the greatest variability with a median of 78% and a range between 37% and 137% of the shear wave speed. The 2013 Craig (137%V_s) and 2018 Palu (125%V_s) events propagated in the unstable supers-

hear range, while the 2013 Balochistan (98%V_s), 2018 North of Honduras (95%V_s), and 2020 Caribbean (104%V_s) earthquakes were 'likely' supershear (95–105%V_s; by assuming expected rupture velocity errors in the estimates) and in any case faster than Rayleigh waves.

4. Finally, we presented new scaling relations from short-period backprojections comparable to finite difference methods. Thrust and normal earthquakes showed a similar magnitude-length relationship compared to established 'long-period' relations. Strike-slip events presented a large dispersion but still within the expected uncertainty. Limitations for strike-slip earthquakes were the lack of events with a large moment magnitude ($M_W >\sim 8$) and the underestimation of rupture lengths due to complexities in the rupture, e.g., complex fault systems as observed for the great 2012 Wharton Basin (M_W 8.6) and 2018 Gulf of Alaska (M_W 7.9) earthquakes.

Whereas overall the method has been optimized for near-real-time processing, the array selection and picking of the end of the rupture still need to be done manually, as is the definition of secondary search grids. This paper has presented and analyzed the fault rupture histories for 54 earthquakes, but we intend to continue to analyze future earthquakes with $M_W \geq 7.5$ and depth less than 200 km. These analyses will be made available under the link listed below.

6 Datasets

The catalog of ruptures is included in the supporting information as map views and in machine-readable format (supporting Data Set S1). The automatic earthquake parameters derived from back-projection are also available (supporting Data Set S2). Both datasets are distributed through GFZ data services (https:dx.doi.org/....)

Acknowledgments

The European Integrated Data Archive (EIDA) and IRIS Data Management Centre were used to access waveforms. We also thank the National Research Institute for Earth Science and Disaster Prevention (NIED) for making Hi-net data available. NIED/Hi-net data was obtained with the HinetPy Python package (Tian, 2020). This research was funded by the National Agency for Research and Development (ANID). Scholarship Program: Doctorado Becas Chile (2017-72180166).

References

Aderhold, K., & Abercrombie, R. (2015). Seismic Rupture on an Oceanic–Continental Plate Boundary: Strike-Slip Earthquakes along the Queen Charlotte–Fairweather FaultSeismic Rupture on an Oceanic–Continental Plate Boundary. *Bulletin of the Seismological Society of America*, *105*(2B), 1129–1142.

Agurto-Detzel, H., Font, Y., Charvis, P., Régnier, M., Rietbrock, A., Ambrois, D., ... others (2019). Ridge subduction and afterslip control aftershock distribution of the 2016 Mw 7.8 Ecuador earthquake. *Earth and Planetary Science Letters*, *520*, 63–76.

An, C., & Meng, L. (2016). Application of array backprojection to tsunami prediction and early warning. *Geophysical Research Letters*, *43*(8), 3677–3685.

Andrews, D. (1976). Rupture velocity of plane strain shear cracks. *Journal of Geophysical Research*, *81*(32), 5679–5687.

Archuleta, R. J. (1984). A faulting model for the 1979 Imperial Valley earthquake. *Journal of Geophysical Research: Solid Earth*, *89*(B6), 4559–4585.

Bao, H., Ampuero, J.-P., Meng, L., Fielding, E. J., Liang, C., Milliner, C. W., ... Huang, H. (2019). Early and persistent supershear rupture of the 2018 magnitude 7.5 Palu earthquake. *Nature Geoscience DOI*, *10*.

Bird, P. (2003). An updated digital model of plate boundaries. *Geochemistry, Geophysics, Geosystems*, *4*(3).

Blaser, L., Krüger, F., Ohrnberger, M., & Scherbaum, F. (2010). Scaling relations of earthquake source parameter estimates with special focus on subduction environment. *Bulletin of the Seismological Society of America*, *100*(6), 2914–2926.

Bouchon, M., Bouin, M.-P., Karabulut, H., Toksöz, M. N., Dietrich, M., & Rosakis, A. J. (2001). How fast is rupture during an earthquake? New insights from the 1999 Turkey earthquakes. *Geophysical Research Letters*, *28*(14), 2723–2726.

Bouchon, M., Karabulut, H., Bouin, M.-P., Schmittbuhl, J., Vallée, M., Archuleta, R., ... Marsan, D. (2010). Faulting characteristics of supershear earthquakes. *Tectonophysics*, *493*(3-4), 244–253.

Bouchon, M., & Vallée, M. (2003). Observation of long supershear rupture during the magnitude 8.1 Kunlunshan earthquake. *Science*, *301*(5634), 824–826.

Burridge, R. (1973). Admissible speeds for plane-strain self-similar shear cracks with friction but lacking cohesion. *Geophysical Journal International*, *35*(4), 439–455.

Burridge, R., Conn, G., & Freund, L. (1979). The stability of a rapid mode II shear crack with finite cohesive traction. *Journal of Geophysical Research: Solid Earth*, *84*(B5), 2210–2222.

Crowell, B. W., & Melgar, D. (2020). Slipping the Shumagin Gap: A kinematic coseismic and early afterslip model of the Mw 7.8 Simeonof Island, Alaska, earthquake. *Geophysical Research Letters*, *47*(19), e2020GL090308.

738 D'Amico, S., Koper, K. D., Herrmann, R. B., Akinci, A., & Malagnini, L. (2010). Imag-
739 ing the rupture of the Mw 6.3 April 6, 2009 L'Aquila, Italy earthquake using back-
740 projection of teleseismic P-waves. *Geophysical Research Letters*, *37*(3).

741 Das, S., & Aki, K. (1977). A numerical study of two-dimensional spontaneous rupture
742 propagation. *Geophysical journal international*, *50*(3), 643–668.

743 Dunham, E. M., & Archuleta, R. J. (2004). Evidence for a supershear transient during
744 the 2002 Denali fault earthquake. *Bulletin of the Seismological Society of America*,
745 *94*(6B), S256–S268.

746 Duputel, Z., Kanamori, H., Tsai, V. C., Rivera, L., Meng, L., Ampuero, J.-P., & Stock,
747 J. M. (2012). The 2012 Sumatra great earthquake sequence. *Earth and Planetary*
748 *Science Letters*, *351*, 247–257.

749 Feng, T., Meng, L., & Huang, H. (2020). Detecting Offshore Seismicity: Combining Back-
750 projection Imaging and Matched-Filter Detection. *Journal of Geophysical Research:*
751 *Solid Earth*, *125*(8), e2020JB019599.

752 Hayes, G. P., Wald, D. J., & Johnson, R. L. (2012). Slab1.0: A three-dimensional model
753 of global subduction zone geometries. *Journal of Geophysical Research: Solid Earth*,
754 *117*(B1).

755 Heidarzadeh, M., Murotani, S., Satake, K., Takagawa, T., & Saito, T. (2017). Fault size and
756 depth extent of the Ecuador earthquake (Mw 7.8) of 16 April 2016 from teleseismic

and tsunami data. *Geophysical Research Letters*, *44*(5), 2211–2219.

Hill, E. M., Borrero, J. C., Huang, Z., Qiu, Q., Banerjee, P., Natawidjaja, D. H., ... others (2012). The 2010 Mw 7.8 Mentawai earthquake: Very shallow source of a rare tsunami earthquake determined from tsunami field survey and near-field GPS data. *Journal of Geophysical Research: Solid Earth*, *117*(B6).

Hill, E. M., Yue, H., Barbot, S., Lay, T., Tapponnier, P., Hermawan, I., ... others (2015). The 2012 Mw 8.6 Wharton Basin sequence: A cascade of great earthquakes generated by near-orthogonal, young, oceanic mantle faults. *Journal of Geophysical Research: Solid Earth*, *120*(5), 3723–3747.

Iinuma, T., Hino, R., Kido, M., Inazu, D., Osada, Y., Ito, Y., ... others (2012). Coseismic slip distribution of the 2011 off the Pacific coast of Tohoku Earthquake (M9.0) refined by means of seafloor geodetic data. *Journal of Geophysical Research: Solid Earth*, *117*(B7).

Ishii, M., Shearer, P. M., Houston, H., & Vidale, J. E. (2005). Extent, duration and speed of the 2004 Sumatra–Andaman earthquake imaged by the Hi-Net array. *Nature*, *435*(7044), 933.

Ishii, M., Shearer, P. M., Houston, H., & Vidale, J. E. (2007). Teleseismic P wave imaging of the 26 December 2004 Sumatra-Andaman and 28 march 2005 Sumatra earthquake ruptures using the Hi-net array. *Journal of Geophysical Research: Solid Earth*,

112(B11).

Kanamori, H. (1981). The nature of seismicity patterns before large earthquakes. *Earthquake Prediction*.

Kelleher, J., & Savino, J. (1975). Distribution of seismicity before large strike slip and thrust-type earthquakes. *Journal of Geophysical Research*, *80*(2), 260–271.

Kennett, B., & Engdahl, E. (1991). Traveltimes for global earthquake location and phase identification. *Geophysical Journal International*, *105*(2), 429–465.

Kiser, E., & Ishii, M. (2013). Hidden aftershocks of the 2011 Mw 9.0 Tohoku, Japan earthquake imaged with the backprojection method. *Journal of Geophysical Research: Solid Earth*, *118*(10), 5564–5576.

Kiser, E., & Ishii, M. (2017). Back-projection imaging of earthquakes. *Annual Review of Earth and Planetary Sciences*, *45*, 271–299.

Kiser, E., Ishii, M., Langmuir, C. H., Shearer, P., & Hirose, H. (2011). Insights into the mechanism of intermediate-depth earthquakes from source properties as imaged by back projection of multiple seismic phases. *Journal of Geophysical Research: Solid Earth*, *116*(B6).

Koper, K. D., Hutko, A., & Lay, T. (2011). Along-dip variation of teleseismic short-period radiation from the 11 March 2011 Tohoku earthquake (Mw 9.0). *Geophysical Research Letters*, *38*(21).

795 Krabbenhoeft, A., von Huene, R., Miller, J. J., Lange, D., & Vera, F. (2018). Strike-slip 23
796 January 2018 Mw 7.9 Gulf of Alaska rare intraplate earthquake: Complex rupture of
797 a fracture zone system. *Scientific reports*, *8*(1), 1–9.

798 Krüger, F., & Ohrnberger, M. (2005). Tracking the rupture of the Mw= 9.3 sumatra
799 earthquake over 1,150 km at teleseismic distance. *Nature*, *435*(7044), 937.

800 Lay, T., Ammon, C., Kanamori, H., Koper, K., Sufri, O., & Hutko, A. (2010). Teleseismic
801 inversion for rupture process of the 27 February 2010 Chile (Mw 8.8) earthquake.
802 *Geophysical Research Letters*, *37*(13).

803 Lay, T., Ammon, C. J., Kanamori, H., Yamazaki, Y., Cheung, K. F., & Hutko, A. R. (2011).
804 The 25 October 2010 Mentawai tsunami earthquake (Mw 7.8) and the tsunami hazard
805 presented by shallow megathrust ruptures. *Geophysical Research Letters*, *38*(6).

806 Lay, T., Kanamori, H., Ammon, C. J., Koper, K. D., Hutko, A. R., Ye, L., ... Rushing,
807 T. M. (2012). Depth-varying rupture properties of subduction zone megathrust faults.
808 *Journal of Geophysical Research: Solid Earth*, *117*(B4).

809 Lay, T., Ye, L., Ammon, C. J., & Kanamori, H. (2017). Intraslab rupture triggering
810 megathrust rupture coseismically in the 17 December 2016 Solomon Islands Mw 7.9
811 earthquake. *Geophysical Research Letters*, *44*(3), 1286–1292.

812 Lay, T., Ye, L., Bai, Y., Cheung, K. F., & Kanamori, H. (2018). The 2018 Mw 7.9 Gulf of
813 Alaska earthquake: Multiple fault rupture in the Pacific plate. *Geophysical Research*

Letters, *45*(18), 9542–9551.

Lee, S.-J., Lin, T.-C., Feng, K.-F., & Liu, T.-Y. (2018). Composite megathrust rupture from deep interplate to trench of the 2016 Solomon Islands earthquake. *Geophysical Research Letters*, *45*(2), 674–681.

Liu, Z., Song, C., Meng, L., Ge, Z., Huang, Q., & Wu, Q. (2017). Utilizing a 3D global P-wave tomography model to improve backprojection imaging: A case study of the 2015 Nepal earthquake. *Bulletin of the Seismological Society of America*, *107*(5), 2459–2466.

Madariaga, R. (1977). High-frequency radiation from crack (stress drop) models of earthquake faulting. *Geophysical Journal International*, *51*(3), 625–651.

Madariaga, R. (1983). High frequency radiation from dynamic earthquake. *Ann. Geophys.*, *1*, 17.

Marty, S., Passelègue, F., Aubry, J., Bhat, H., Schubnel, A., & Madariaga, R. (2019). Origin of high-frequency radiation during laboratory earthquakes. *Geophysical Research Letters*, *46*(7), 3755–3763.

Melgar, D., Fan, W., Riquelme, S., Geng, J., Liang, C., Fuentes, M., ... Fielding, E. J. (2016). Slip segmentation and slow rupture to the trench during the 2015, Mw8.3 Illapel, Chile earthquake. *Geophysical Research Letters*, *43*(3), 961–966.

Meng, L., Ampuero, J.-P., Luo, Y., Wu, W., & Ni, S. (2012b). Mitigating artifacts in

833 back-projection source imaging with implications for frequency-dependent properties
834 of the Tohoku-Oki earthquake. *Earth, planets and space*, *64*(12), 5.

835 Meng, L., Ampuero, J.-P., Stock, J., Duputel, Z., Luo, Y., & Tsai, V. (2012a). Earth-
836 quake in a maze: Compressional rupture branching during the 2012 Mw 8.6 Sumatra
837 earthquake. *Science*, *337*(6095), 724–726.

838 Meng, L., Bao, H., Huang, H., Zhang, A., Bloore, A., & Liu, Z. (2018). Double pincer
839 movement: Encircling rupture splitting during the 2015 Mw 8.3 Illapel earthquake.
840 *Earth and Planetary Science Letters*, *495*, 164–173.

841 Meng, L., Huang, H., Bürgmann, R., Ampuero, J. P., & Strader, A. (2015). Dual megathrust
842 slip behaviors of the 2014 Iquique earthquake sequence. *Earth and Planetary Science*
843 *Letters*, *411*, 177–187.

844 Meng, L., Inbal, A., & Ampuero, J.-P. (2011). A window into the complexity of the
845 dynamic rupture of the 2011 Mw 9 Tohoku-Oki earthquake. *Geophysical Research*
846 *Letters*, *38*(7).

847 Meng, L., Zhang, A., & Yagi, Y. (2016). Improving back projection imaging with a novel
848 physics-based aftershock calibration approach: A case study of the 2015 Gorkha earth-
849 quake. *Geophysical Research Letters*, *43*(2), 628–636.

850 Mogi, K. (1969). Some feature of recent seismic acrivity in and near Japan (2): Activity
851 before and after great earthquakes. *Bull. Earthq. Res. Inst., Univ. Tokyo*, *47*, 395–

417.

Moreno, M., Li, S., Melnick, D., Bedford, J., Baez, J., Motagh, M., ... others (2018). Chilean megathrust earthquake recurrence linked to frictional contrast at depth. *Nature Geoscience*, *11*(4), 285–290.

Moreno, M., Melnick, D., Rosenau, M., Baez, J., Klotz, J., Oncken, O., ... others (2012). Toward understanding tectonic control on the Mw 8.8 2010 Maule Chile earthquake. *Earth and Planetary Science Letters*, *321*, 152–165.

Neidell, N. S., & Taner, M. T. (1971). Semblance and other coherency measures for multichannel data. *Geophysics*, *36*(3), 482–497.

Palo, M., Tilmann, F., Krueger, F., Ehlert, L., & Lange, D. (2014). High-frequency seismic radiation from Maule earthquake (Mw 8.8, 2010 February 27) inferred from high-resolution backprojection analysis. *Geophysical Journal International*, *199*(2), 1058–1077.

Rawlinson, N., & Kennett, B. L. (2004). Rapid estimation of relative and absolute delay times across a network by adaptive stacking. *Geophysical Journal International*, *157*(1), 332–340.

Robinson, D., Das, S., & Searle, M. (2010). Earthquake fault superhighways. *Tectonophysics*, *493*(3-4), 236–243.

Rössler, D., Krueger, F., Ohrnberger, M., & Ehlert, L. (2010). Rapid characterisation of

large earthquakes by multiple seismic broadband arrays. *Natural Hazards and Earth System Sciences*, *10*(4), 923–932.

Ruppert, N., Rollins, C., Zhang, A., Meng, L., Holtkamp, S., West, M., & Freymueller, J. (2018). Complex faulting and triggered rupture during the 2018 Mw 7.9 offshore Kodiak, Alaska, earthquake. *Geophysical Research Letters*, *45*(15), 7533–7541.

Santellanes, S. R., Melgar, D., Crowell, B. W., & Lin, J.-T. (2021). Potential megathrust co-seismic slip during the 2020 Sand Point, Alaska strike-slip earthquake. *Earth and Space Science Open Archive*, 15.

Satriano, C., Kiraly, E., Bernard, P., & Vilotte, J.-P. (2012). The 2012 Mw 8.6 Sumatra earthquake: Evidence of westward sequential seismic ruptures associated to the reactivation of a N-S ocean fabric. *Geophysical Research Letters*, *39*(15).

Schurr, B., Asch, G., Hainzl, S., Bedford, J., Hoechner, A., Palo, M., ... others (2014). Gradual unlocking of plate boundary controlled initiation of the 2014 Iquique earthquake. *Nature*, *512*(7514), 299.

Schurr, B., Moreno, M., Tréhu, A. M., Bedford, J., Kummerow, J., Li, S., & Oncken, O. (2020). Forming a Mogi doughnut in the years prior to and immediately before the 2014 M8.1 Iquique, northern Chile, earthquake. *Geophysical Research Letters*, *47*(16), e2020GL088351.

Simons, M., Minson, S. E., Sladen, A., Ortega, F., Jiang, J., Owen, S. E., ... others (2011).

The 2011 magnitude 9.0 Tohoku-Oki earthquake: Mosaicking the megathrust from seconds to centuries. *science*, *332*(6036), 1421–1425.

Sippl, C., Moreno, M., & Benavente, R. (2020). Microseismicity appears to outline highly coupled regions on the Central Chile megathrust. *EarthArXiv*.

Socquet, A., Hollingsworth, J., Pathier, E., & Bouchon, M. (2019). Evidence of supershear during the 2018 magnitude 7.5 Palu earthquake from space geodesy. *Nature Geoscience*, *12*(3), 192.

Spudich, P., & Cranswick, E. (1984). Direct observation of rupture propagation during the 1979 Imperial Valley earthquake using a short baseline accelerometer array. *Bulletin of the Seismological Society of America*, *74*(6), 2083–2114.

Strollo, A., Cambaz, D., Clinton, J., Danecek, P., Evangelidis, C. P., Marmureanu, A., ... et al. (2021, Mar). EIDA: The European Integrated Data Archive and Service Infrastructure within ORFEUS. *Seismological Research Letters*, *92*(3), 1788–1795. Retrieved from `http://dx.doi.org/10.1785/0220200413` doi: 10.1785/0220200413

Styron, R., & Pagani, M. (2020). The GEM global active faults database. *Earthquake Spectra*, *36*(1_suppl), 160–180.

Tadapansawut, T., Okuwaki, R., Yagi, Y., & Yamashita, S. (2021). Rupture process of the 2020 caribbean earthquake along the oriente transform fault, involving supershear rupture and geometric complexity of fault. *Geophysical Research Letters*, *48*(1),

e2020GL090899.

Taymaz, T., Ganas, A., Yolsal-Çevikbilen, S., Vera, F., Eken, T., Erman, C., ... others (2021). Source Mechanism and Rupture Process of the 24 January 2020 Mw 6.7 Doğanyol–Sivrice Earthquake obtained from Seismological Waveform Analysis and Space Geodetic Observations on the East Anatolian Fault Zone (Turkey). *Tectonophysics*, *804*, 228745.

Tian, D. (2020, March). *seisman/hinetpy: 0.6.6.* Zenodo. Retrieved from `https://doi.org/10.5281/zenodo.3695076` doi: 10.5281/zenodo.3695076

Tilmann, F., Zhang, Y., Moreno, M., Saul, J., Eckelmann, F., Palo, M., ... others (2016). The 2015 Illapel earthquake, central Chile: A type case for a characteristic earthquake? *Geophysical Research Letters*, *43*(2), 574–583.

Twardzik, C., & Ji, C. (2015). The Mw7.9 2014 intraplate intermediate-depth Rat Islands earthquake and its relation to regional tectonics. *Earth and Planetary Science Letters*, *431*, 26–35.

Vallée, M., & Doeut, V. (2016). A new database of source time functions (STFs) extracted from the SCARDEC method. *Physics of the Earth and Planetary Interiors*, *257*, 149-157. doi: 10.1016/j.pepi.2016.05.012

Walker, K. T., Ishii, M., & Shearer, P. M. (2005). Rupture details of the 28 March 2005 Sumatra Mw 8.6 earthquake imaged with teleseismic P waves. *Geophysical Research*

Letters, *32*(24).

Walker, K. T., & Shearer, P. M. (2009). Illuminating the near-sonic rupture velocities of the intracontinental Kokoxili Mw 7.8 and Denali fault Mw 7.9 strike-slip earthquakes with global P wave back projection imaging. *Journal of Geophysical Research: Solid Earth*, *114*(B2).

Wang, K., Huang, T., Tilmann, F., Peacock, S. M., & Lange, D. (2020). Role of Serpentinized Mantle Wedge in Affecting Megathrust Seismogenic Behavior in the Area of the 2010 M = 8.8 Maule Earthquake. *Geophysical Research Letters*, *47*(22), e2020GL090482.

Wells, D. L., & Coppersmith, K. J. (1994). New empirical relationships among magnitude, rupture length, rupture width, rupture area, and surface displacement. *Bulletin of the seismological Society of America*, *84*(4), 974–1002.

Xie, Y., & Meng, L. (2020). A Multi-Array Back-Projection Approach for Tsunami Warning. *Geophysical Research Letters*, *47*(14), e2019GL085763.

Yao, H., Gerstoft, P., Shearer, P. M., & Mecklenbräuker, C. (2011). Compressive sensing of the Tohoku-Oki Mw 9.0 earthquake: Frequency-dependent rupture modes. *Geophysical Research Letters*, *38*(20).

Yao, H., Shearer, P. M., & Gerstoft, P. (2013). Compressive sensing of frequency-dependent seismic radiation from subduction zone megathrust ruptures. *Proceedings of the Na-*

tional Academy of Sciences, *110*(12), 4512–4517.

Ye, L., Lay, T., & Kanamori, H. (2014). The 23 June 2014 Mw 7.9 Rat Islands archipelago, Alaska, intermediate depth earthquake. *Geophysical Research Letters*, *41*(18), 6389–6395.

Ye, L., Lay, T., & Kanamori, H. (2020). Anomalously low aftershock productivity of the 2019 Mw 8.0 energetic intermediate-depth faulting beneath Peru. *Earth and Planetary Science Letters*, *549*, 116528.

Ye, L., Lay, T., & Kanamori, H. (2021). The 25 march 2020 m_w 7.5 Paramushir, northern Kuril Islands earthquake and major ($m_w \geq 7.0$) near-trench intraplate compressional faulting. *Earth and Planetary Science Letters*, *556*, 116728. doi: 10.1016/j.epsl.2020.116728

Yin, J., Yang, H., Yao, H., & Weng, H. (2016). Coseismic radiation and stress drop during the 2015 Mw 8.3 Illapel, Chile megathrust earthquake. *Geophysical Research Letters*, *43*(4), 1520–1528.

Yue, H., Lay, T., Freymueller, J. T., Ding, K., Rivera, L., Ruppert, N. A., & Koper, K. D. (2013). Supershear rupture of the 5 January 2013 Craig, Alaska (Mw 7.5) earthquake. *Journal of Geophysical Research: Solid Earth*, *118*(11), 5903–5919.

Zeng, H., Wei, S., & Wu, W. (2019). Sources of uncertainties and artefacts in back-projection results. *Geophysical Journal International*, *220*(2), 876-891.